Politecnico di Milano
School of Industrial and Information Engineering

Department of Physics

Master of Science in Engineering Physics

Phonons in a *ferroelectric* superconductor: optical spectroscopy on $Ca_xSr_{1-x}TiO_{3-\delta}$

Thesis advisor:
Prof. Giacomo Claudio Ghiringhelli

Thesis coadvisor:
Prof. Dirk van der Marel

Thesis tutor:
Dr. Carl Willem Rischau

Candidate:
Francesco Barantani
Student ID n. 877222

Academic Year 2017–2018

UNIVERSITÉ
DE GENÈVE

FACULTY OF SCIENCE
Department of Quantum
Matter Physics

The whole work presented in these pages was carried out at the Department of Quantum Matter Physics of the University of Geneva, under the supervision of Prof. Dirk van der Marel and Dr. Willem Rischau.

To my family

Will you understand what I'm going to tell you? [...]
No, you're not going to be able to understand it. [...]
That is because I don't understand it. Nobody does.

R. Feynman – QED: The Strange Theory of Light and Matter

Contents

Abstract **III**

Sommario **IV**

Introduction **VI**

1 Introduction to strontium titanate **1**
1.1 Superconductivity in strontium titanate 3
1.1.1 History 3
1.1.2 Electron doping of STO 4
1.1.3 n-doped STO 4
1.2 Ferroelectricity in strontium titanate 5
1.3 Coexistence of superconducting and ferroelectric phases . . . 6
1.3.1 Ferroelectric-like order 6
1.3.2 The quantum critical scenario 7

2 Theory **9**
2.1 Ferroelectricity 9
2.1.1 Phonons and ferroelectricity 12
2.2 Superconductivity 14
2.2.1 Basics of BCS theory 15
2.2.2 Formalism of BCS theory 17
2.3 Theory of quantum criticality 19
2.3.1 Quantum critical scenario in strontium titanate 20

3 Introduction to optical spectroscopy **22**
3.1 Electromagnetic fields in media[39] 22
3.1.1 Optical conductivity and dielectric function 24
3.2 Fresnel equations 24

3.3 Drude Lorenz model . . . 25
3.4 Kramers-Kronig relations and sum rules . . . 26
3.4.1 Optical Kramers-Kronig relations . . . 28
3.4.2 Sum rules . . . 29
3.5 RefFit . . . 30
3.6 FT-IR spectroscopy . . . 30

4 Experimental setups **32**
4.1 Spectrometer . . . 32
4.1.1 Sources and beamsplitter . . . 34
4.2 Detectors . . . 35
4.2.1 Bolometers 1.6 and 4.2 K . . . 35
4.2.2 MCT . . . 36
4.3 Cryostat and gold evaporator . . . 36
4.4 Measurement procedure . . . 37
4.5 THz transmissivity . . . 39
4.6 Raman spectroscopy . . . 40

5 Experimental Measurements **41**
5.1 $SrTiO_3$ spectroscopy . . . 42
5.1.1 Temperature dependence of reflectivity . . . 42
5.1.2 THz transmissivity and MIR transmissivity . . . 43
5.2 $Ca_xSr_{1-x}TiO_{3-\delta}$ optical spectroscopy: reflectivity spectra . . . 45
5.3 Raman measurements . . . 47

6 Discussion of results **49**
6.1 Phonon analysis: temperature scan . . . 49
6.1.1 $SrTiO_3$ . . . 50
6.1.2 $Ca_xSr_{1-x}TiO_3$: insulating samples . . . 52
6.1.3 $Ca_xSr_{1-x}TiO_{3-\delta}$: electron-doped samples . . . 53
6.2 Spectral Weight and effective charge . . . 54
6.2.1 $SrTiO_3$ . . . 56
6.2.2 $Ca_xSr_{1-x}TiO_3$: insulating samples . . . 57
6.2.3 $Ca_xSr_{1-x}TiO_{3-\delta}$: electron-doped samples . . . 58
6.3 Effective mass . . . 59

Conclusions and future outlook **62**

Bibliography **64**

Acknowledgements **69**

Abstract

Strontium titanate $SrTiO_3$ is a quantum paraelectric insulator. A ferroelectric order can be stabilized by chemical or isotopic substitution. Moreover, upon electron doping, the material can also be turned into a metal, which become superconducting at temperatures around 300 mK. So far, the superconducting pairing mechanism remains unknown.
In 2017, the coexistence of a ferroelectric and superconducting phase was discovered in $Ca_xSr_{1-x}TiO_{3-\delta}$, accompanied by an enhancement of the critical temperature with respect to the non-ferroelectric $SrTiO_3$. The aim of this work is to improve the knowledge of the phonons in this material in order to help to find new perspectives for the pairing mechanism.
In this work, IR spectroscopy measurements on $SrTiO_3$ and $Ca_xSr_{1-x}TiO_{3-\delta}$ will be presented. Their temperature dependence will be analysed and the changes arising upon Ca substitution will be discussed.
From the experimental data, the optical conductivity of the samples will be computed using a Drude-Lorentz model for the dielectric function and Kramers-Kronig relations. This quantity gives new information on the phonons of this material and also microscopic information such as the effective mass of the free carriers in the metallic samples.

Sommario

Il titanato di stronzio ($SrTiO_3$) è un materiale isolante (con un gap di 3.22 eV), appartenente al gruppo delle perovskiti, che mostra un comportamento paraelettrico quantistico.
Nel titanato di stronzio è possibile stabilizzare la fase ferroelettrica con sostituzione chimica (Sr con Ca) o isotopica (di ossigeno). In caso di drogaggio di tipo elettronico, il materiale diventa metallico e mostra uno stato superconduttore al di sotto di circa 300 mK. Il meccanismo che dà origine alla superconduttività nel titanato di stronzio rimane ignoto, nonostante in questo materiale essa sia nota già dagli anni '60.
Nel 2017 è stata scoperta la coesistenza della fase ferroelettrica e superconduttiva nel $Ca_xSr_{1-x}TiO_{3-\delta}$, la cui temperatura critica è maggiore rispetto a quella del titanato di stronzio; tale fenomeno può esser spiegato utilizzando una teoria critica quantistica, in cui il fonone ferroelettrico riveste un ruolo chiave.

L'obiettivo del presente lavoro è di migliorare la conoscenza dei fononi nel $Ca_xSr_{1-x}TiO_{3-\delta}$, in modo da poter discutere lo scenario quanto-critico e favorire la ricerca di un meccanismo di superconduttività nel titanato di stronzio.

In questo progetto vengono presentate le misure di spettroscopia infrarosse e Raman sui campioni di $SrTiO_3$ and $Ca_xSr_{1-x}TiO_{3-\delta}$. Inoltre è analizzata la loro dipendenza rispetto alla temperatura e sono discussi i cambiamenti che derivano dalla sostituzione dello stronzio con il calcio.

Dai dati sperimentali è possibile trovare la conduttività ottica dei campioni, calcolandola attraverso le relazioni di Kramers-Kronig e utilizzando un modello di Drude-Lorentz per la funzione dielettrica. La conduttività ottica permette infatti di approfondire la conoscenza dei fononi nel materiale, in

particolare del modo ferroelettrico.
Dal peso spettrale è possible estrarre anche altre informazioni microscopiche come la massa efficace degli elettroni nel caso di campioni metallici.

Introduction

The aim of this work is to study the phonon properties in strontium titanate $SrTiO_3$ and Ca-substituted strontium titanate $Ca_xSr_{1-x}Ti\,O_{3-\delta}$.

$SrTiO_3$ is a perovskite material which presents an indirect gap of 3.22eV. It is a quantum paraelectric with a very large dielectric permittivity.
Upon very low electron-doping, strontium titanate becomes metallic and presents a superconducting ground state at temperatures around 300mK; furthermore the critical temperature shows a dome shape as a function of the carrier density. The pairing mechanism is still under debate, despite the fact that the superconductivity in this material is known since the 60s, thus remaining a challenge for theory.
A ferroelectric order can be stabilized in $SrTiO_3$ by chemical (Ca for Sr) or isotopic (^{18}O for ^{16}O) substitution, with Curie temperatures up to around 30 K.
The coexistence of a ferroelectric and superconducting phases was discovered in $Ca_xSr_{1-x}TiO_{3-\delta}$ in 2017. The higher superconducting critical temperatures with respect to the non-ferroelectric material $SrTiO_{3-\delta}$ can be explained in a quantum critical scenario, where the ferroelectric soft phonon plays an important role.

In this work, FT-IR spectroscopy has been used to measure temperature dependent reflectivity spectra of $SrTiO_3$ and $Ca_xSr_{1-x}TiO_{3-\delta}$. Complementary Raman measurements has been taken on $Ca_xSr_{1-x}TiO_{3-\delta}$ samples at low temperatures.

The experimental spectra have been fitted using a Drude-Lorentz model for the dielectric complex function. By using Kramers-Kronig relations, optical conductivity has been computed and compared to the one from the fits in the case of $SrTiO_3$.

The temperature analysis at 10 and 300 K of the real part of the optical conductivity has given new information on the phonons of the samples and new insights on the soft phonon. Its behaviour can then be compared to the model assumed in the quantum critical scenario.

On the other hand, from the spectral weight it is possible to find the effective mass of the free carriers in the metallic samples and discuss the results with previous studies.

CHAPTER 1

Introduction to strontium titanate

Strontium titanate ($SrTiO_3$) is an oxide crystallising in a *perovskite* structure.
Perovskite materials can be described by the form ABO_3. In their unit cell, the A-type atoms occupy the corner positions (e.g. $(0,0,0)$) while the B-type atoms sit on the body-centered positions (e.g. $(\frac{1}{2},\frac{1}{2},\frac{1}{2})$) and the oxygen atoms on the face-centered positions (e.g. $(\frac{1}{2},\frac{1}{2},0)$). As shown in figure 1.1, the oxygen atoms sit on the corners of octahedra. The cubic lattice parameter a is 3.905Å.

$SrTiO_3$ (STO) undergoes a so-called anti-ferrodistortive transition (AFD) around 105 K which leads the system to a new geometry: the crystal structure changes from cubic (O_1^h) to tetragonal (D_{18}^{4h}). The origin of this structural phase transition lies in the antiphase rotation of the TiO_6 octahe-

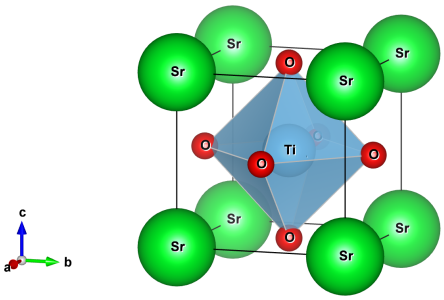

Figure 1.1: Unit cell of $SrTiO_3$

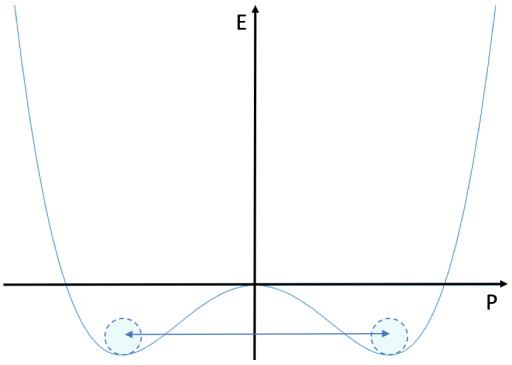

Figure 1.2: Double well potential with tunneling between two minima, where P is the polarization and E is the free energy.

dra. From a study of specific heat near the critical temperature [1], this phase transition was shown to be second-order, mean-field and close to tricriticality.

STO is a band gap insulator (with $E_{gap} = 3.2$eV). From band calculations [2], the indirect gap turns out to be at the Γ-point. The filled bands are those related to O $2p$ orbitals, while three empty bands can be associated to Ti $3d$ orbitals.

It is a paraelectric material, i.e. with decreasing temperature, the dielectric constant increases following a Curie law until about 40K [3] and then it saturates at a very high level (~ 23000) below $\sim$ 5K [3].
The huge value of the dielectric constant at low temperature means that it becomes very easy to align the dipoles by applying an external field as the lattice polarizability is high.
In the case of STO this phenomenon is called *quantum paraelectricity* (or *incipient ferroelectricity*) because quantum fluctuations or 0K-fluctuations prevent the material from becoming ferroelectric. In fact it is possible to imagine the energy landscape as a usual double-well potential where the system cannot stay in one of the two minima: due to quantum fluctuations it tunnels in between them and it does not find stable configuration, as represented in figure 1.2.
The incipient ferroelectricity can be found in the softening [1] of a zone-center phonon mode (TO1[2]), which remains incomplete (it does not reach zero frequency) even at 0K, thus leading to the aforementioned instability i.e. quantum paraelectricity. The softening of the TO1 mode was observed by

[1] A mode is called soft if its frequency decreases with decreasing temperature. The opposite case is called a hard mode.
[2] The expression TO mode stands for transverse optical mode.

Raman [4] and neutron [5] scattering.

Moreover, it is known that in polar crystals the Lyddane-Sachs-Teller (LST) expression holds, which relates the static electric permittivity $\epsilon(0)$ and the ratio of frequency of the transverse (TO) and longitudinal (LO) optical modes as follows:

$$\frac{\epsilon(0)}{\epsilon_\infty} = \left(\frac{\omega_{\mathrm{LO}}}{\omega_{\mathrm{TO}}}\right)^2 \tag{1.1}$$

In the case of the soft mode, this relation was experimentally verified [5].

1.1 Superconductivity in strontium titanate

1.1.1 History

In 1964, semiconducting STO (slightly electron-doped) was found to become superconducting already at very low carrier densities with maximum critical temperatures (T_c) of around 300mK [6]. This was the discovery of the first oxide perovskite superconductor and one the first semiconducting superconductors. In the 80s, it was found that the critical temperature presents a dome shape as a function of the carrier density, as reported in figure 1.3. Such superconducting domes have been discovered later in many other ma-

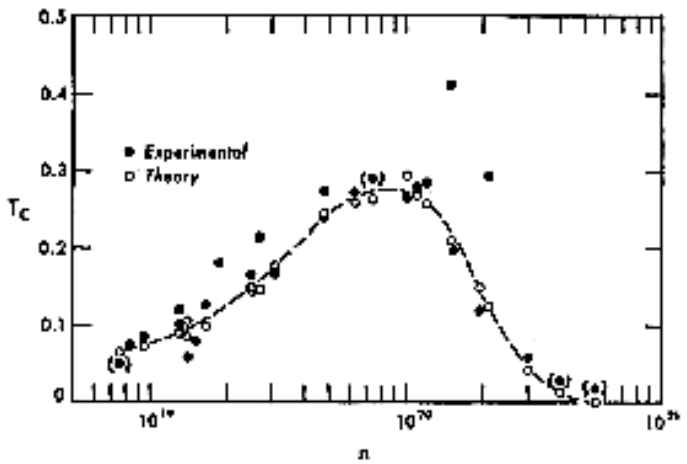

Figure 1.3: Critical temperature T_c of $SrTiO_3$ as a function of the carrier concentration n [7]. The values of T_c were determined by magnetic susceptibility measurements.

terials such as high temperature superconductors.
Despite the early date of the discovery of superconductivity in STO, the pairing mechanism is still under discussion today and so far there is no agreement on the theory lying behind it. In fact, already in the 1960s there

was a theory based on multi-valley electron-phonon coupling which was able to reproduce the experimental data with a good success [8]. However, experimental fermiology studies [9] later showed that STO is not a multi-valley electronic system.
For a few years the interest in STO superconductivity faded out, due to the low critical temperature (for applications), until 2004 when the existence of a 2D-electron gas at the interface between $SrTiO_3$-$LaAlO_3$ was discovered [10]. Another study in 2007 led to the discovery of superconductivity in this 2D electron gas [11] and it renewed the interest in the field of research of STO due to new properties of these heterostructure interfaces.

Moreover, it is worth underlining that n-doped STO is, by far, the most dilute superconductor as it shows a superconducting state already at an electron density of $n \simeq 5.5 \times 10^{17}\text{cm}^{-3}$ [9].

1.1.2 Electron doping of STO

First of all, in order to have a superconducting STO it is necessary to electron-dope the insulating material. It is possible to do so in different ways:

- removing a small fraction of oxygen, i.e., $SrTiO_{3-\delta}$,
- substituting Ti with Nb, i.e., $SrNb_xTi_{1-x}O_3$,
- substituting Sr with La, i.e., $La_xSr_{1-x}TiO_3$.

In order to remove oxygen, it is possible to anneal the insulating sample under vacuum at temperatures around $700 - 1200°\text{C}$; depending on the duration and the temperature more or less oxygen is removed. This doping is n-type as the oxidation state of oxygen is -2 and when O is removed, the material gains those two electrons. On the other hand, with Nb substitution it is possible to gain only one electron as well as with La.
In this work, only samples doped by oxygen removal will be measured.

1.1.3 n-doped STO

Electron-doped $SrTiO_3$ was studied intensively because of the discovery of its superconducting ground state. It can be interesting to review some of the properties of $SrTiO_{3-\delta}$.
The metallicity appears at electron densities of the order $10^{16} - 10^{17}\text{cm}^{-3}$, which means $\delta \sim 10^{-5}$ i.e. one out of 100000 oxygen atoms was removed[3].

[3] We can relate the electron density to δ considering that each oxygen removed contributes with 2 electrons:

$$n = \frac{2}{\Omega}\delta \tag{1.2}$$

where $\Omega = a^3$ is the volume of the unit cell and a is the lattice parameter.

Such a low doping level can be explained by thinking of the effective Bohr radius[4], which turns out to be around 600 nm for metallic strontium titanate [12], where the high value of the dielectric constant plays a major role. Exploiting the Mott criterion for a metal-insulator transition, the lowest carrier concentration to find a metallic behaviour is 10^{11}cm^{-3} [13] (it is not observable due to extrinsic impurities).
As shown in previous works [9], the Fermi surface is almost spherical and it is located at the center of the Brillouin zone; it grows in size as the doping level increases up to a limit level. Three concentric bands are subsequently filled as the carriers concentration increases, as reported in [14]; it is thus possible to define two critical doping levels when electrons start to fill the following band.
It is also known that at the optimal carrier concentration, the superconducting gap(s) is(are) s-wave and nodeless [15], since it is not clear if there are two superconducting bands.
Another strange characteristic of $SrTiO_{3-\delta}$ is that, for $n = 5.5 \times 10^{17}\text{cm}^{-3}$ with a critical temperature $T_c = 86\text{mK}$, its Fermi temperature $T_F = 13\text{K}$ is much smaller than the Debye temperature $\Theta_D = 400\text{K}$. In standard BCS theory, the assumption is $T_F \gg \Theta_D$: this means that applying BCS theory to strontium titanate is not straightforward.

1.2 Ferroelectricity in strontium titanate

As discussed above, insulating STO is a quantum paraelectric characterised by a very large dielectric constant at low temperatures.
We also know that the stability of the perovskite structure is very sensible to relative ionic radii, which means that if a cation is substituted with a different atom there will be distorted equilibrium positions with lower symmetry. This is the case if Sr is substituted with Ca: comparing ionic radii, it turns out that it is larger for strontium ($r_i = 132\text{pm}$) than for calcium ($r_i = 114\text{pm}$).
So, if just a small part of Sr atoms is substituted with Ca, from structure calculations it is possible to see that the equilibrium position of Ca atoms is off-center [16]. This distortion creates a local net dipole and due to the huge dielectric constant the material undergoes a ferroelectric phase transition [17]: polarization clusters grow in size with decreasing temperature and their percolation at the Curie temperature leads to a long-range ferroelectric order. Another way to understand the stabilization of ferroelectric order is

[4] By definition, the effective Bohr radius is

$$a_B = \frac{4\pi\epsilon(0)\hbar^2}{m^* e^2} \tag{1.3}$$

where $\epsilon(0)$ is the static dielectric permettivity and m^* the effective mass.

the damping of quantum fluctuations due to Ca substitution.
It is possible to describe the competition between quantum fluctuations and the ferroelectric order by a transverse Ising model [18]: the Ca atoms increase the barrier in the double well potential suppressing the tunnelling between the two ferroelectric minima.

It is also possible to obtain the same behaviour by substituting Sr with Ba instead of Ca [19] or by isotopic substitution of oxygen of ^{16}O with ^{18}O [20] or by applying stress [21] or under electric field [22].

Now, let us focus on Ca-substituted STO, i.e. $Ca_xSr_{1-x}TiO_3$.
Concerning its phase diagram, different structural phases are present, depending on the Ca concentration [23].
From previous studies [17], it is known that a stable ferroelectric ground state can emerge only if $0.002 < x < 0.02$. Within this range, the Curie temperature (T_C) of the ferroelectric transition increases with increasing x between 0 and 32K. The shown ferroelectricity is XY-type, with the polarization along the [110] and [110] directions [24].

1.3 Coexistence of superconducting and ferroelectric phases

In 2017 it has been discovered that the ferroelectric and superconducting phases in $Ca_xSr_{1-x}TiO_{3-\delta}$ can coexist [25]. This is quite surprising since usually, in order to have a ferroelectric behaviour, the material has to be insulating (to have a net polarization); whereas superconductors require mobile electrons.

Regarding other examples for the coexistence of the three orders: ferromagnetism, superconductivity (SC) and ferroelectricity (FE), so far a ferromagnetic superconductor (UGe_2, in 2000) [26] and a ferroelectric ferromagnet ($EuTiO_3$ under large biaxial compressive strain, in 2010) [27] had been discovered. The recent observation of coexistence of SC and FE in $Ca_xSr_{1-x}TiO_{3-\delta}$ was the first report of a ferroelectric superconductor.
As shown in figure 1.4, the recent results [25] showed that not only the two phases coexist, but that the superconducting critical temperature is larger in the case of $Ca_xSr_{1-x}TiO_{3-\delta}$ for carrier concentrations between $4 \times 10^{18} cm^{-3}$ and $3 \times 10^{19} cm^{-3}$.

1.3.1 Ferroelectric-like order

As seen above, a ferroelectric material is a material which shows a spontaneous electric polarization, i.e. it presents net electric dipoles which can

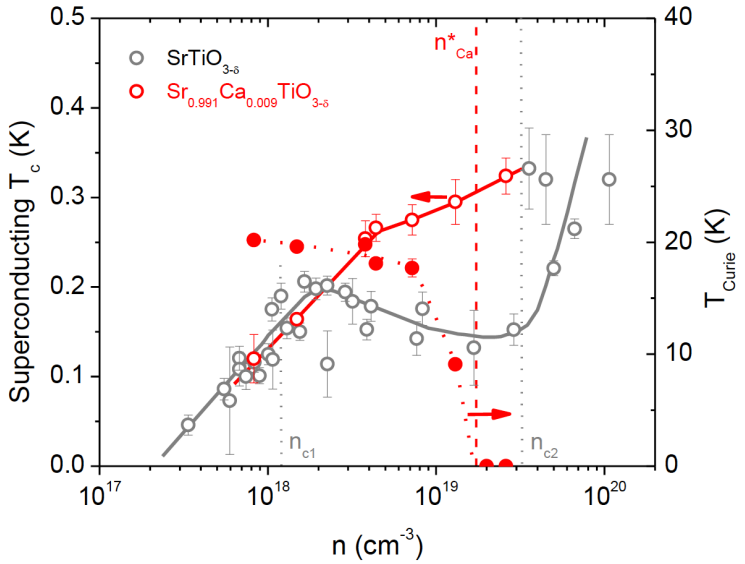

Figure 1.4: Curie temperature T_{Curie} (filled circles, right scale) and critical temperature T_c (open circles, left scale) for $Ca_xSr_{1-x}TiO_{3-\delta}$ compared to critical temperature of $SrTiO_3$, as a function of the electron density n [25].

align all in the same direction. A necessary condition for this to be true is that the material has to be an insulator, otherwise free electrons will *screen* the net dipoles present in the structure.
On the other hand, in superconductors it is necessary to have mobile electrons so that they can pair up to form Coopers pairs.
Thus, it is not proper to speak of ferroelectric order in $Ca_xSr_{1-x}TiO_{3-\delta}$, but it is more appropriate to call it *ferroelectric-like* order, since the phase transition is structurally indistinguishable from the ferroelectric one, but there is no reversible polarization.
In these $Ca_xSr_{1-x}TiO_{3-\delta}$ sample, it is possible to find anomalies in resistivity measurements near the corresponding Curie temperature of the insulating samples. Furthermore, Raman spectroscopy showed the same hardening of the ferroelectric soft mode below the Curie temperature T_C for the insulating and metallic samples [25].
For a given Ca concentration, the temperature of the anomaly decreases as the carrier concentration increases, suggesting that electrons are destroying the ferroelectric-like order.

1.3.2 The quantum critical scenario

In 2014 Rowley et al. [28] proposed the idea of ferroelectric quantum criticality to explain the enhancement of the superconducting critical temperature from the measurements on $SrTi(^{18}O^{16}_{x}O_{1-x})_3$ [20]. In a following work [29],

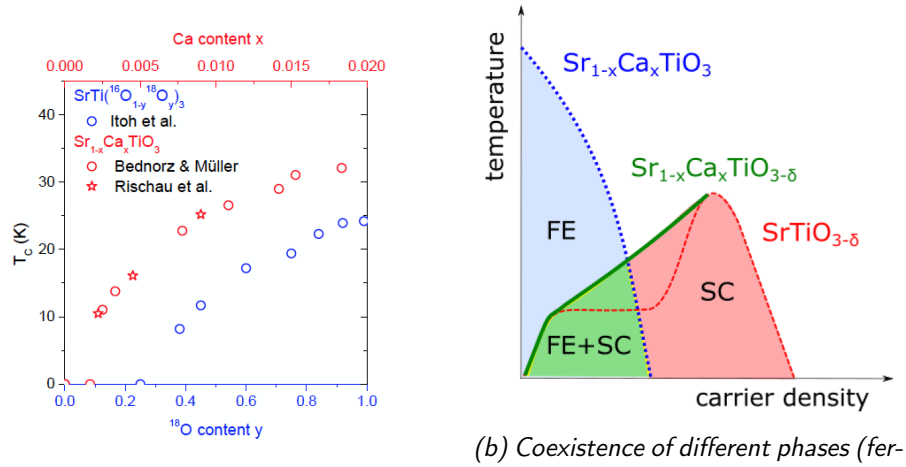

(a) Curie temperature of $SrTi(^{18}O^{16}_{x}O_{1-x})_3$ and $Ca_xSr_{1-x}TiO_{3-\delta}$, from [15].

(b) Coexistence of different phases (ferroelectric) and $Ca_xSr_{1-x}TiO_{3-\delta}$ compared to critical temperature of $SrTiO_3$, as a function of the electron density, from [15].

Figure 1.5: Quantum critical scenario.

it was proposed a relation between the maximum critical temperature and the presence of the soft mode related to the ferroelectric instability.

Focusing on the case of isotopic substitution $SrTi(^{18}O^{16}_{x}O_{1-x})_3$, the value $x = 35\%$ was found to be the quantum critical point [28], i.e. when the system undergoes the ferroelectric transition at 0 K. Moreover, an anomalous isotope effect of the superconducting critical temperature [30] was found in $SrTi(^{18}O^{16}_{x}O_{1-x})_{3-\delta}$: the experimental coefficient $\alpha = 10$ [5] has the opposite sign and larger magnitude with respect to the $\alpha_{BCS} = -0.5$ from BCS theory.

A similar enhancement of the critical temperature was reported in the case of $Ca_xSr_{1-x}TiO_{3-\delta}$ [25], as explained above. The scenario is analogous to the quantum criticality of the isotopic substitution and it could be possible to use the model [29] to explain the experimental measurements, although some theoretical assumptions need to be better justified, which will be discussed in the following chapters.

Figure 1.5a compares the Curie temperatures for isotopic and Ca substitution in STO, while figure 1.5a represents the coexistence of ferroelectric and superconducting phase in $Ca_xSr_{1-x}TiO_{3-\delta}$, as discussed in [25].

[5] It is possible to define α as follows:

$$\alpha = \frac{d \ln T_c}{d \ln M} \tag{1.4}$$

d where T_c is the critical temperature and M the isotope mass.

CHAPTER 2

Theory

As discussed in the previous chapter, there are two relevant phase transitions in $Ca_xSr_{1-x}TiO_{3-\delta}$ [25]: the ferroelectric phase transition and the superconducting one. Now, let us introduce these two important phase transitions.

2.1 Ferroelectricity

A material is said to be ferroelectric if it shows a spontaneous polarization, which can be reversed by applying an external electric field; the polarization will follow a hysteresis loop. These analogies with ferromagnetism explain the origin of word *ferro* in the definition of ferroelectricity. The first ferroelectric material was found in the 1920s in Rochelle salt [31]. Then, in the 1940s the field of ferroelectrics quickly developed and in the 1960s many ferroelectric materials were discovered; after that, many theoretical studies were done, leading to new applications.
Although ferroelectricity is, besides certain aspects, similar to ferromagnetism, its late discovery with respect to ferromagnetic materials (permanent magnets were already known by Greek and Chinese more than 2000 years ago) is a sign of their deep differences.
In fact, while in ferromagnetism the spontaneous magnetization is mainly given by the spin magnetic moments, in ferroelectric materials the electric dipoles are responsible of the polarization, so the point is to understand why there are internal electric dipoles and when they begin to align in the same direction.
The total polarization ($\boldsymbol{P}$) is given by the sum of local dipole moments con-

tributions ($\boldsymbol{p}_i$)

$$\boldsymbol{P} = \sum_i \boldsymbol{p}_i \text{ with } \boldsymbol{p}_i = q_i \boldsymbol{r}_i \tag{2.1}$$

where it is possible to model each dipole moment as two point-like charges q at a distance $\boldsymbol{r}$.
Analogously to ferromagnetism, the Curie temperature (T_C) can be defined for the ferroelectric phase transition, below which the long-range order forces win over short-range fluctuations (i.e. thermal fluctuations). Moreover, if T_C is near 0K, quantum fluctuations start to become important since they compete with long-range order preventing the material from becoming ferroelectric (as in the case of strontium titanate). In the latter case, the material is called a quantum paraelectric or incipient ferroelectric.

It is possible to treat ferroelectricity using the Landau-Ginzburg-Devonshire theory (LGD), where the polarization P is considereds as the order parameter. So, the Gibbs energy (in the uniaxial case) reads [32]

$$G = F - EP = F_0 + \frac{\alpha}{2}P^2 + \frac{\beta}{4}P^4 + \frac{\gamma}{6}P^6 - EP \tag{2.2}$$

where F_0 is the free energy density of the paraelectric state, α, β, γ are parameters depending on temperature and pressure and E is the electric field.
If the transition is second-order, then $\beta > 0$ and $\gamma = 0$, while the parameter α can be written as a function of the Curie temperature and the Weiss constant C[1]

$$\alpha = \frac{1}{\epsilon_0 C}(T - T_C) \tag{2.4}$$

since it changes sign crossing T_C (there are two new stable minima). Minimising the Gibbs energy, one finds that

$$P_s = \pm\sqrt{-\frac{\alpha}{\beta}} = \pm\sqrt{\frac{1}{\epsilon_0 \beta C}(T_C - T)} \tag{2.5}$$

where the double sign represents the two orientations of the polarization. In the case of a first order transition, the parameters are

$$\alpha = \frac{1}{\epsilon_0 C}(T - T_0), \quad \beta < 0, \quad \gamma > 0 \tag{2.6}$$

[1]We recall the Weiss law for the susceptibility χ:

$$\chi = \frac{C}{T - T_C} \tag{2.3}$$

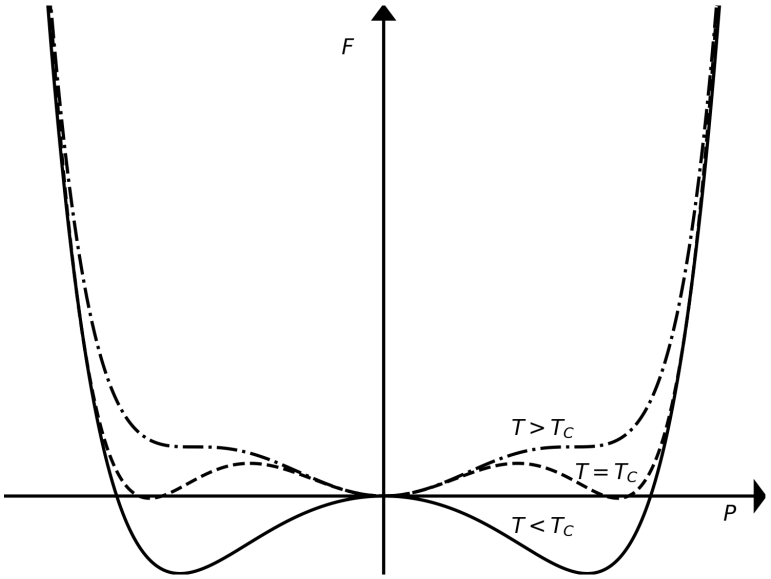

Figure 2.1: Free energy expansion as a function of polarization P, according to LGD theory.

where T_0 represents the temperature at which the two polarizations are the only two stable configurations, while we define T_C when we have three minima, as represented in figure 2.1.
Assuming $E = 0$, it is possible to compute T_C

$$F = \frac{\alpha}{2}P^2 + \frac{\beta}{4}P^4 + \frac{\gamma}{6}P^6 = 0 \tag{2.7}$$

where the solutions are

$$\begin{gathered} P = 0 \\ P = \pm\sqrt{\frac{1}{4\gamma}(-3\beta + \sqrt{9\beta^2 - 48\gamma\alpha})} \end{gathered} \tag{2.8}$$

which means that

$$\alpha = \frac{3\beta^2}{16\gamma} \quad \text{i.e.} \quad T_C = T_0 + \frac{3\epsilon_0 C\beta^2}{16\gamma} \tag{2.9}$$

From the previous equations, for $T = T_C$ the polarization shows a jump of $\Delta P = \sqrt{-\frac{3\beta}{4\gamma}}$.
Below the Curie temperature, the stable configurations are two and as in eq. 2.5 they can be computed minimising the total energy

$$P_s = \pm\sqrt{-\frac{\beta}{2\gamma}\Big(1 - \sqrt{1 - \frac{4\alpha\gamma}{\beta^2}}\Big)} \tag{2.10}$$

From LGD theory the critical exponent of a mean field theory is found since

$$P = \sqrt{-\frac{1}{\epsilon_0 C\beta}(T_C - T)} \simeq |T - T_C|^{\beta} \tag{2.11}$$

with $\beta = \frac{1}{2}$.

This simple model does not strictly apply to oxide perovskites such as $BaTiO_3$ or $PbTiO_3$ [33] where also the order parameter represented by the displacement between cations (Ba/Pb and Ti) has to be considered. In fact, in these materials, crystal structural changes are the causes of spontaneous polarization and since the structure from cubic, for instance, becomes tetragonal it is important to take into account the strain (u); thus the energy expansion now reads

$$G = F_0 + \frac{\alpha}{2}P^2 + \frac{\beta}{4}P^4 + \frac{\gamma}{2}u^2 + \delta P^2 u \tag{2.12}$$

where γ represents the Hooke's law and δ the coupling between strain and polarization.
A mean field approximation was assumed, which means that the forces are infinitely long-range. It can be considered a good approximation because in ferroelectrics, mainly Coulomb interactions are present which are effectively long-range. So we could use critical exponents from mean-field theory in this context.

2.1.1 Phonons and ferroelectricity

Let us introduce the concept of phonons, i.e. lattice vibrations of crystal, with a microscopic approach [34].
Let us first consider a 1D monoatomic chain, composed by identical atoms of mass m connected by springs (of elastic constant k) and uniformly spaced at a distance a in the equilibrium position. It is possible to write the equation of motion for the n^{th} atom, in the harmonic approximation:

$$m\frac{\partial^2 u_n}{\partial t^2} = k(u_{n+1} - u_n) + k(u_{n-1} - u_n) \tag{2.13}$$

where u_n is the displacement of the n^{th} atom. One can guess a solution in the form

$$u_n(t) = u_0 e^{i(qx_n - \omega(q)t)} \tag{2.14}$$

which, substituted in eq. 2.13, gives:

$$\begin{aligned} -m\omega^2(q)e^{i(qx_n-\omega(q)t)} = k\big[&e^{i[q(x_n+a)-\omega(q)t]} + \\ &+ e^{i[q(x_n-a)-\omega(q)t]} - e^{i[qx_n-\omega(q)t]}\big] \end{aligned} \tag{2.15}$$

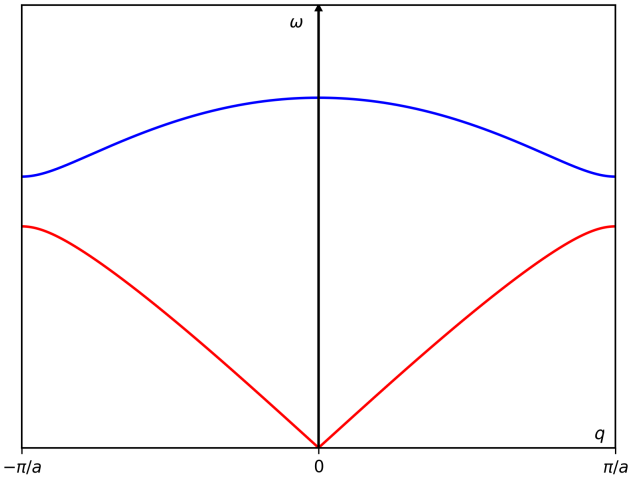

Figure 2.2: Dispersion relation for the diatomic linear chain.

thus leading to the form

$$m\omega^2(q) = 2k\big[1 - \cos(qa)\big] = 4k\sin^2\big(\frac{qa}{2}\big) \tag{2.16}$$

It is possible to find the dispersion relation $\omega(q)$ of this vibration:

$$\omega(q) = 2\sqrt{\frac{k}{m}}\sin\big(\frac{qa}{2}\big) \tag{2.17}$$

This mode, whose frequency goes linearly to zero as the wavevector q approaches 0, is called an acoustic mode, since it behaves similarly to a sound wave. Usually the dispersion relation is represented in the interval $\big(-\frac{\pi}{a}, \frac{\pi}{a}\big)$, as in figure 2.2. Moreover, Born-van Karman boundary condition ($u(0) = u(Na)$) requires

$$e^{iqNa} = 1 \rightarrow q = \frac{2\pi n}{Na} \tag{2.18}$$

From this, it is possible to see that for a 1D linear chain with N atoms N normal modes exist.
If then a linear chain with a diatomic basis is considered, $2N$ normal modes exist, but only half of them are acoustic. In fact in the dispersion relation two branches are present: the acoustic one (red), as above, and the optical mode (blue), which has a finite frequency for $q = 0$, as shown in figure 2.2.

In order to describe the vibrations of a complex solid, it is necessary to consider a 3D lattice with a basis. Then, $3p$ different modes exist, where p is the number of atoms of the basis; only 3 of them are acoustic, while

the remaining $3(p-1)$ modes are optical. In a 3D structure, the dispersion relation becomes more complicated, since the wavevector $\boldsymbol{q}$ is a vector along 3 directions in the reciprocal space inside the Brillouin zone.
Furthermore in a 3D isotropic lattice, it is also possible to distinguish between transverse and longitudinal modes: in a longitudinal mode, the vibrations occur along the direction of propagation, while for a transverse mode, they are perpendicular to the wavevector $\boldsymbol{q}$.

We can link an optical phonon to the ferroelectric transition considering that when the structure freezes off-center below the Curie temperature, the frequency of the phonon goes to zero for $q = 0$.
In fact, the displacement u_{opt} can be related to the polarization through the expression

$$P = \frac{1}{V_{uc}}\left[e^* u_{opt} + o(u_{opt}^3)\right] \tag{2.19}$$

where e^* is the effective charge related to the microscopic dipole moment.
Assuming the harmonic approximation, in eq. 2.2 the free energy expansion (without an external electric field) can be written as a function of the displacement u_{opt} and used to write the equation of motion

$$m\frac{\partial^2 u_{opt}}{\partial t^2} = -\frac{\partial F}{\partial u_{opt}} \sim -\alpha(T) u_{opt} \tag{2.20}$$

which is equivalent to say that

$$\omega_{q=0} \sim |T - T_C|^{1/2} \tag{2.21}$$

This is a *soft phonon* because its frequency decreases with decreasing temperature. It is thus possible to exploit the frequency of the soft phonon to describe the properties of a material which undergoes a ferroelectric transition [35].

2.2 Superconductivity

Superconductivity and ferroelectricity are more or less equal in age, in fact we can fix 1911 as the discovery of superconductivity when Kamerlingh Onnes succeeded in producing liquid helium and observed that the resistivity of mercury drops to zero when the temperature is below 4.2K [36].
The second main effect of superconductivity was discovered in 1933 by Ochsenfeld and Meissner when they observed that superconductors expel a magnetic field (the effect is now known as *Meissner* effect). Besides these experimental evidences, the first theory which managed to describe superconductivity was formulated by the London brothers in 1935.
We have to wait until 1950 for the phenomenological Ginzburg-Landau theory [37] and 1957 for the BCS theory[38]. The first one was able to describe

macroscopic properties of superconductors and also to predict the division into type-I and type-II[2]. On the other hand, the BCS theory was the first microscopic theory which explained the mechanism of superconductivity of some materials. Let us focus on this theory.

2.2.1 Basics of BCS theory

In 1957 Bardeen, Cooper and Schrieffer formulated a theory (which later become known as *BCS theory*) which was able to describe microscopically what happens in the superconducting (SC) state.
The main idea of BCS theory is that in the SC state electrons form pairs mediated by the exchange of a phonon (i.e. lattice vibration): the so-called Cooper pairs; below the critical temperature they condensate in the same state, since these quasi-particles are bosons[3].
Electron-phonon interaction is the crucial quantity which plays a major role: when the formation of Cooper pairs is favoured, then the material undergoes the transition to the SC state.

Let us first study the problem with a semi-classical approach, to show that electrons near Fermi surface are unstable with respect to formation of Cooper pairs.[4]
Now let us consider two electrons near the Fermi surface with fixed momenta $\boldsymbol{p}_{1,2}$ (knowing that $\boldsymbol{p}_{1,2} = \hbar \boldsymbol{k}_{1,2}$) interacting via a phonon of energy $E_{ph} = \hbar\omega_D$; then it is possible to write:

$$\begin{aligned} \boldsymbol{k}_1 + \boldsymbol{k}_2 &= \boldsymbol{k} \\ E_F \leq E_{1,2} &\leq E_F + \hbar\omega_D \\ |k_F| \leq |k_{1,2}| &\leq |k_F| + |\Delta k| \end{aligned} \tag{2.22}$$

where ω_D is the Debye frequency (i.e. the maximum frequency of a phonon, due to the lattice). As shown in the figure 2.3, the Fermi spheres of the two electrons have the maximum overlap if $\boldsymbol{k}_1 = -\boldsymbol{k}_2$ which means that the electrons have opposite momenta.
Now let us write the Schrodinger equation for these two electrons

$$-\frac{\hbar^2}{2m}(\nabla_1^2 + \nabla_2^2)\Psi(\boldsymbol{r}_1, \boldsymbol{r}_2) + V(\boldsymbol{r}_1, \boldsymbol{r}_2)\Psi(\boldsymbol{r}_1, \boldsymbol{r}_2) = E\Psi(\boldsymbol{r}_1, \boldsymbol{r}_2) \tag{2.23}$$

where $V(\boldsymbol{r}_1, \boldsymbol{r}_2)$ is the potential and E the eigenvalue such that $E = 2E_F + \epsilon$, with $\epsilon < 0$ when we gain energy from the formation of the pair.

[2] In type-I superconductors, there is no magnetic field inside the material in the superconducting state, while in type-II the superconducting state can present vortices where the external magnetic field is not expelled.

[3] The Cooper pair has spin 0 or 1, due to the fact that electrons are fermions (with spin 1/2).

[4] This is the so-called Cooper problem.

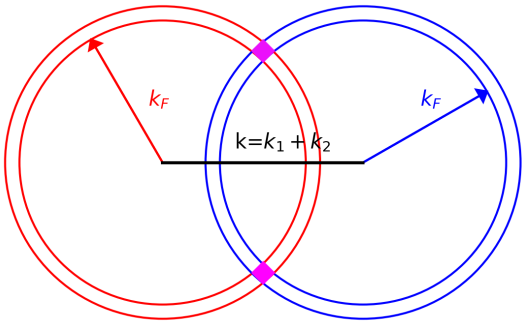

Figure 2.3: Two Fermi spheres of interacting electrons.

Since these electrons can be considered nearly free particles with opposite momentum (of modulus k), we can write the wavefunction as

$$\Psi(\boldsymbol{r}_1, \boldsymbol{r}_2) = \frac{1}{L^3} \sum_{\boldsymbol{k}} g(\boldsymbol{k}) e^{i\boldsymbol{k}\cdot(\boldsymbol{r}_1 - \boldsymbol{r}_2)} \tag{2.24}$$

where $g(\boldsymbol{k})$ is the combined density of states, which reads

$$g(\boldsymbol{k}) = \begin{cases} 0 & \text{for} \quad |\boldsymbol{k}| < k_F \\ 0 & \text{for} \quad |\boldsymbol{k}| > k_F + \Delta k = \sqrt{\frac{2m}{\hbar^2}(E_F + \hbar\omega_D)} \\ 2\rho(k_F) & \text{for} \quad |\boldsymbol{k}| \simeq k_F \end{cases} \tag{2.25}$$

Substituing the expression 2.24 into equation 2.23, we find

$$\frac{\hbar^2}{2m} g(\boldsymbol{k}) + \frac{1}{L^3} \sum_{\boldsymbol{k}'} g(\boldsymbol{k}') V_{\boldsymbol{k}\boldsymbol{k}'} = (2E_F + \epsilon) g(\boldsymbol{k}) \tag{2.26}$$

where $V_{\boldsymbol{k}\boldsymbol{k}'}$ represents the different contributions to the potential from electrons with different momenta[5].
Let us do an important approximation: let us assume that only the electrons near the Fermi surface feel an attractive constant potential (it can be justified taking into account many-body effects) i.e.

$$V_{\boldsymbol{k}\boldsymbol{k}'} = \begin{cases} -V_0 & \text{for} \quad E_F \leq \frac{\hbar^2 k^2}{2m} \leq E_F + \hbar\omega_D \\ 0 & \text{otherwise} \end{cases} \tag{2.28}$$

With this approximation, the energy gain (or loss) ϵ of the pair can be computed:

$$g(k) = -\frac{1}{L^3} \frac{\sum_{k'} g(k') V_0}{2E_F - \frac{\hbar^2 k^2}{m} + \epsilon} \tag{2.29}$$

[5]Formally, we can write

$$V_{\boldsymbol{k}\boldsymbol{k}'} = \int V(\boldsymbol{r}_1, \boldsymbol{r}_2) e^{i(\boldsymbol{k}-\boldsymbol{k}')\cdot(\boldsymbol{r}_1 - \boldsymbol{r}_2)} d\boldsymbol{r}_1 d\boldsymbol{r}_2 \tag{2.27}$$

and considering that the density of states (g(k)) near the Fermi energy is more or less the same at the Fermi surface ($\rho(E_F + \xi) \simeq \rho(E_F)$), then:

$$1 = \frac{V_0}{L^3} \sum_{k'} \frac{1}{2\xi - \epsilon} \tag{2.30}$$

where $\xi = \frac{\hbar^2 k^2}{m} - 2E_F$ represents the energy of the phonon. Turning the sum into an integral, with constant density of states ($\rho(E_F)$) and assuming that the energy of the phonon can vary up to the Debye energy $\hbar\omega_D$, it reads:

$$1 = V_0 \rho(E_F) \int_0^{\hbar\omega_D} \frac{1}{2\xi - \epsilon} d\xi = \frac{1}{2} V_0 \rho(E_F) \ln \frac{\epsilon - 2\hbar\omega_D}{\epsilon} \tag{2.31}$$

Finally, the expression for ϵ can be found, which reads:

$$\epsilon = \frac{2\hbar\omega_D}{1 - e^{\frac{2}{V_0 \rho(E_F)}}} \simeq -2\hbar\omega_D e^{-\frac{1}{V_0 \rho(E_F)}} \tag{2.32}$$

where the last expression is correct in the weak interaction regime (i.e. $V_0\rho(E_F) \ll 1$). Eventually, it is possible to define the coupling parameter $\lambda = V_0\rho(E_F)$.

2.2.2 Formalism of BCS theory

As seen above, already from a semiclassical approach in the weak interaction limit the formation of Cooper pair near the Fermi energy is energetically favoured. Now, it can be interesting to discuss what happens with more than one pair. To do so, the tools of second quantization can be exploited. In fact the generic state can be written as:

$$|\psi\rangle = u_k |0\rangle_k + v_k |1\rangle_k \tag{2.33}$$

where u_k represents the probability that the Cooper state is unoccupied while v_k that it is occupied ($|u_k|^2 + |v_k|^2 = 1$).
Let us now define the creation and annihilation operators for Cooper pair respectively $\hat{\sigma}_k^\dagger$ and $\hat{\sigma}_k$[6]. Assuming non-interacting Cooper pairs, the ground state can be written as

$$|\Psi_{\text{BCS}}\rangle = \prod_k (u_k |0\rangle_k + v_k |1\rangle_k) \tag{2.35}$$

[6] These operators act on the state as

$$\begin{aligned} \hat{\sigma}_k^\dagger |0\rangle_{k'} &= |1\rangle_k \delta_{kk'} \qquad & \hat{\sigma}_k |0\rangle_{k'} &= |0\rangle_k \delta_{kk'} \\ \hat{\sigma}_k^\dagger |1\rangle_{k'} &= |1\rangle_k \delta_{kk'} \qquad & \hat{\sigma}_k |1\rangle_{k'} &= |0\rangle_k \delta_{kk'} \end{aligned} \tag{2.34}$$

As seen above, two electrons with opposite momenta are paired and from symmetry considerations it is possible to show that, in order to have a constant energy gain, the electrons have also opposite spins.
Now let us consider the scattering between two pairs, which can be represented as

$$(\boldsymbol{k}\uparrow, -\boldsymbol{k}\downarrow) \Longleftrightarrow (\boldsymbol{k'}\uparrow, -\boldsymbol{k'}\downarrow) \tag{2.36}$$

In term of operators, the interacting hamiltonian can be written as

$$H^i = -\frac{V_0}{L^3}\sum_{k,k'}\frac{1}{2}\hat{\sigma}^\dagger_{k'}\hat{\sigma}_k \tag{2.37}$$

from which the energy reduction due to scattering can be computed

$$\langle\Psi_{\mathrm{BCS}}|H^i|\Psi_{\mathrm{BCS}}\rangle = -\frac{V_0}{L^3}\sum_{k,k'} v_k u_{k'} v_{k'} u_k \tag{2.38}$$

The total energy is given by the sum of the kinetic energy and the interaction energy:

$$W_{\mathrm{BCS}} = H^k + H^v = 2\sum_k v_k^2\xi_k - \frac{V_0}{L^3}\sum_{k,k'} v_k u_{k'} v_{k'} u_k \tag{2.39}$$

and, since $|v_k|^2 + |u_k|^2 = 1$, the coefficients can be written as $v_k = \cos\theta_k$ and $u_k = \sin\theta_k$. Following the variational approach, the energy has to be minimised to find the ground state:

$$\frac{\partial W_{\mathrm{BCS}}}{\partial\theta_k} = -2\sin 2\theta_k\xi_k - \frac{V_0}{L^3}{\sum_k}' \sin 2\theta_{k'}\cos 2\theta_{k'} = 0 \tag{2.40}$$

defining $\Delta = \frac{V_0}{L^3}\sum_{k'} u_{k'}v_{k'} = \frac{V_0}{2L^3}\sum_{k'}\sin 2\theta_{k'}$, it becomes

$$\tan 2\theta_k = -\frac{\Delta}{\xi_k} \tag{2.41}$$

This leads to the expression:

$$\begin{aligned}\sin 2\theta_k &= 2u_k v_k = -\frac{\Delta}{\sqrt{\xi_k^2+\Delta^2}}\\ \cos 2\theta_k &= u_k^2 - v_k^2 = \frac{\xi_k}{\sqrt{\xi_k^2+\Delta^2}}\end{aligned} \tag{2.42}$$

which is analogous to write:

$$v_k^2 = \frac{1}{2}\left(1 - \frac{\xi_k}{\sqrt{\xi_k^2+\Delta^2}}\right) \tag{2.43}$$

Eventually the expression for the coefficient v_k has been found, so the ground state energy reads:

$$W^0_{\mathrm{BCS}} = \sum_k \xi_k \left(1 - \frac{\xi_k}{\sqrt{\xi_k^2 + \Delta^2}}\right) - \frac{V_0}{L^3}\Delta^2 \tag{2.44}$$

Moreover, it is possible to show that there exists an energy gap which has to be overcome to break one pair. With the previous approach, the gapped quasiparticles energy reads

$$E_k = \sqrt{\xi_k^2 + \Delta^2} \tag{2.45}$$

It is possible to generalise the treatment also for temperature different from 0 K, thus considering also Fermi-Dirac distribution. From BCS formula for the energy gap, it is possible to compute the critical temperature (T_c) of the superconducting transition (at which the system is gapless):

$$T_c = \frac{2e^\gamma}{\pi}\frac{\hbar\omega_D}{k_B}e^{-1/\lambda} \tag{2.46}$$

where γ is Euler-Mascheroni constant ($\gamma \simeq 0.577$), ω_D is the Debye frequency and λ is the coupling constant[7].

2.3 Theory of quantum criticality

First of all, let us introduce the concept of quantum critical point (QCP). Depending on a given parameter (such as the concentration of calcium or of O^{18}), the system is at its quantum critical point when a phase transition occurs at zero temperature. This means that by tuning the parameter it is possible to bring the system toward its QCP.
At zero temperature, only quantum fluctuations are present, due to zero point energy; on the other hand at a finite temperature, we have also thermal fluctuations ($\simeq k_B T$). So the system feels quantum fluctuations also at a finite (but small) temperature until they become comparable to thermal fluctuations, as we see in the figure 2.4. If, for instance, there are two tuning parameters, in the phase diagram a quantum critical line can be identified. In this project the tuning parameters are the Ca concentration and the n-doping . As explained in the following chapter, the $Ca_xSr_{1-x}TiO_{3-\delta}$ presents the coexistence of ferroelectric and superconducting phase only for

[7] In the BCS theory, the coupling constant λ can be written as

$$\lambda = \rho(E_F)V_0 \tag{2.47}$$

where the density of states at the Fermi energy ($\rho(E_F)$) and the electron-phonon potential (V_0) are both constant.

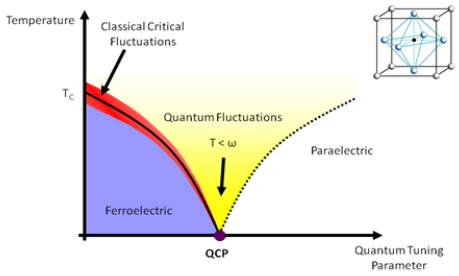

Figure 2.4: Phase diagram in proximity of a quantum critical point.

x between $(0.002, 0.009)$ and n-doping between $(3 \times 10^{17}, 10^{19})$.

Now let us consider a *BCS-like* theory, where the bosons responsible of Cooper pairs are the quantum fluctuations, and let us assume that the coupling constant λ depends on the energy of the boson

$$\lambda = \lambda(\omega) \tag{2.48}$$

In the weak-coupling approximation we can study how the critical temperature changes depending on the boson energy

$$\frac{dT_c}{d(\hbar\omega)} = Be^{-1/\lambda}\left(1 - \frac{\hbar\omega}{[\lambda(\omega)]^2}\frac{d\lambda(\omega)}{d(\hbar\omega)}\right) \tag{2.49}$$

Then, in the case of a power-law dependence of $\lambda(\omega)$

$$\lambda(\omega) = \frac{A}{(\hbar\omega)^\alpha} \tag{2.50}$$

the previous derivative reads

$$\frac{dT_c}{d(\hbar\omega)} = Be^{-1/\lambda}\left(1 - \alpha\frac{(\hbar\omega)^{2\alpha}}{A}\right) \tag{2.51}$$

From this expression we see that the critical temperature attains its maximum for

$$\hbar\omega = \left(\frac{A}{\alpha}\right)^{\frac{1}{2\alpha}} \tag{2.52}$$

and also that for large energy the critical temperature remains more or less constant and goes to 0.

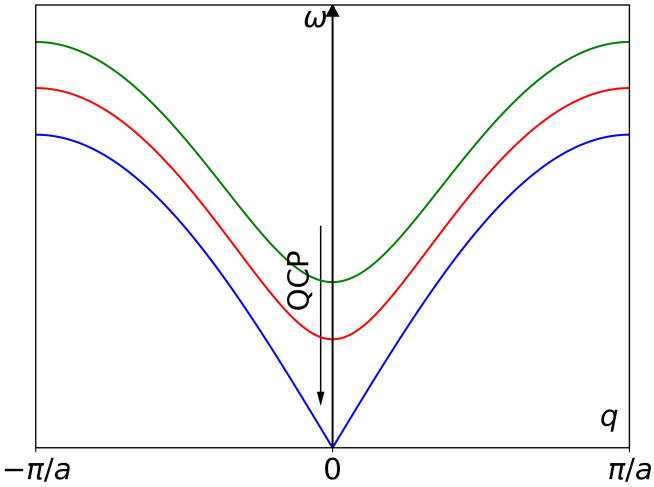

Figure 2.5: Dispersion relation typical of a mode describing a quantum phase transition, whose frequency goes to zero as it approaches the quantum critical point.

2.3.1 Quantum critical scenario in strontium titanate

In [29], a precise model was used to link theory and experimental data.
The coupling constant was chosen inversely proportional to the frequency (i.e. with the previous α taken equal to one) of the soft mode, written as a function of the quantum critical parameters:

$$\lambda = \frac{\alpha^2}{\omega_{\boldsymbol{q}=0(x,n)}} \tag{2.53}$$

where α is considered to be constant, x and n are respectively the Ca concentration and the carriers density.

Thus, integrating for all the contributions in the first Brillouin zone, a more precise expression of the coupling constant can be derived:

$$\lambda \simeq \int_{-\pi}^{+\pi} \frac{dq}{2\sqrt{\Gamma}\sqrt{\Gamma - \cos q}} \tag{2.54}$$

where the dispersion relation at the denominator is typical of a ferroelectric soft mode, since Γ can be written as a function of the quantum critical parameters x and n, and it is represented in figure 2.5.
Having an expression for λ, it is possible to insert it in the gap equation in order to find the critical temperature:

$$\frac{2\pi^2}{\lambda} = \int_{-E_F}^{0} \frac{N(\epsilon)}{\epsilon} \tanh\left(\frac{\epsilon}{2T_c}\right) d\epsilon \tag{2.55}$$

Thus, in [29] a BCS-like theory was developed, considering the soft phonon as the coupling phonon. The arbitrary dependence of Γ was then fitted to the experimental points from the measurements on $SrTi^{18}O_3$ [20], in order to follow the dome shape.

CHAPTER 3

Introduction to optical spectroscopy

In order to study and discuss the validity of the quantum critical scenario, it is necessary to have experimental data which can be related to theoretical quantities. To measure experimental data in this work optical spectroscopy has been exploited.
Optical spectroscopy deals with all the techniques related to reflection or transmission of light. In order to study the bulk properties it is necessary to use light with energy comparable to bulk structural excitations such as *phonons*: this means infrared light.
In this case, since we want to have an analysis depending on the frequency (so on the energy) to see the different excitations, FT-IR spectroscopy can be performed.

3.1 Electromagnetic fields in media[39]

First of all, let us recall Maxwell's equations

$$\begin{aligned} \nabla \cdot \boldsymbol{D} &= \rho \\ \nabla \times \boldsymbol{E} &= -\frac{\partial \boldsymbol{B}}{\partial t} \\ \nabla \cdot \boldsymbol{B} &= 0 \\ \nabla \times \boldsymbol{H} &= \boldsymbol{j} + \frac{\partial \boldsymbol{D}}{\partial t} \end{aligned} \tag{3.1}$$

where $\boldsymbol{D}$ is the displacement field, $\boldsymbol{E}$ the electric field, $\boldsymbol{B}$ the magnetic induction, $\boldsymbol{H}$ the magnetic field and $\boldsymbol{j}$ the current density.

We know that in general these fields are related by constitutive relations:

$$\begin{aligned} \boldsymbol{D} &= \epsilon_0 \boldsymbol{E} + \boldsymbol{P} \\ \boldsymbol{B} &= \mu_0 \boldsymbol{H} + \boldsymbol{M} \\ \boldsymbol{j}_c &= \sigma \boldsymbol{E} \end{aligned} \tag{3.2}$$

where ϵ_0 is the vacuum permittivity while μ_0 the vacuum permeability, $\boldsymbol{P}$ the polarization field, $\boldsymbol{M}$ the magnetization field and $\boldsymbol{j}_c$ is the conduction current density, which is related to the total current density by $\boldsymbol{j} = \boldsymbol{j}_0 + \boldsymbol{j}_c$ where $\boldsymbol{j}_0$ is the source current density. Here we already find one of the most important quantity: the conductivity σ.

Moreover in general we can write that

$$\begin{aligned} \boldsymbol{P} &= \chi_e \boldsymbol{E} \\ \boldsymbol{M} &= \chi_m \boldsymbol{H} \end{aligned} \tag{3.3}$$

where χ_e and χ_m are respectively the electric and magnetic susceptibility tensors. If then we restrict our study only to linear material, tensorial relations become scalar and we can write

$$\begin{aligned} \boldsymbol{D} &= \epsilon_0 \epsilon_r \boldsymbol{E} \\ \boldsymbol{B} &= \mu_o \mu_r \boldsymbol{H} \end{aligned} \tag{3.4}$$

where respectively ϵ_r and μ_r are the relative dielectric and magnetic constant, which can be directly related to susceptibilities.
Taking the curl of the second and the fourth equations in eq. 3.1 and assuming to be source-free ($\boldsymbol{\rho} = 0$ and $\boldsymbol{j}_0 = 0$) in a linear and homogeneous medium, we find

$$\begin{aligned} \nabla^2 \boldsymbol{E} &= \mu\sigma \frac{\partial \boldsymbol{E}}{\partial t} + \mu\epsilon \frac{\partial^2 \boldsymbol{E}}{\partial t^2} \\ \nabla^2 \boldsymbol{B} &= \mu\sigma \frac{\partial \boldsymbol{B}}{\partial t} + \mu\epsilon \frac{\partial^2 \boldsymbol{B}}{\partial t^2} \end{aligned} \tag{3.5}$$

where $\epsilon = \epsilon_0 \epsilon_r$ and $\mu = \mu_0 \mu_r$.
If now we look for plane wave solution, i.e. $\boldsymbol{E}(\boldsymbol{r}, t) = \boldsymbol{E}_0 e^{i(\boldsymbol{k}\cdot\boldsymbol{r} - \omega t)}$, where $\boldsymbol{E}_0$ is perpendicular to the wavevector $\boldsymbol{k}$ and ω is the wave frequency, we can write:

$$k^2 = \frac{\omega^2}{c^2}(\epsilon_r + i\frac{\sigma}{\epsilon_0 \omega})\mu_r = k_0^2 \tilde{n}^2 \tag{3.6}$$

where k_0 is the wavevector in the vacuum, $\tilde{n}$ is the complex refractive index, which can be written as

$$\tilde{n}^2 = \tilde{\epsilon}\tilde{\mu} = (\epsilon_1 + i\epsilon_2)(\mu_1 + i\mu_2) \tag{3.7}$$

So far, the treatment is completely general (except multiferroics), but now we will restrict our model to non-magnetic material, which means $\mu_r = 1$ (as it is in the case of $SrTiO_3$).

3.1.1 Optical conductivity and dielectric function

As seen above, in general we can write $\tilde{\epsilon} = \epsilon_1 + i\epsilon_2$ and the material response can depend on the frequency. Because of this, we can recast our starting equations:

$$\begin{aligned} \boldsymbol{D} &= \epsilon_0 \epsilon_1 \boldsymbol{E} \\ \boldsymbol{j}_c &= \sigma_1 \boldsymbol{E} \end{aligned} \tag{3.8}$$

From eq. 3.6 we see that the dielectric function becomes

$$\tilde{\epsilon} = \epsilon_1 + i\frac{\sigma_1}{\epsilon_0 \omega} \tag{3.9}$$

where its imaginary part reads

$$\epsilon_2 = \frac{\sigma_1}{\epsilon_0 \omega} \tag{3.10}$$

Similarly we can also think that the optical conductivity may be written as $\sigma(\omega) = \sigma_1(\omega) + i\sigma_2(\omega)$, then from the fourth Maxwell's equation in Fourier space we find

$$\begin{aligned} \nabla \times \boldsymbol{H} &= \sigma_1 \boldsymbol{E} - i\omega\epsilon_0\epsilon_1 \boldsymbol{E} + \omega\epsilon_0 \boldsymbol{E} - \omega\epsilon_0 \boldsymbol{E} \\ \nabla \times \boldsymbol{H} &= [\sigma_1 + i\omega\epsilon_0(1 - \epsilon_1)]\boldsymbol{E} - i\omega\epsilon_0 \boldsymbol{E} \end{aligned} \tag{3.11}$$

where the imaginary part of the conductivity reads

$$\sigma_2 = \omega\epsilon_0(1 - \epsilon_1) \tag{3.12}$$

From these relations, we can write the relation between $\tilde{\sigma}$ and $\tilde{\epsilon}$, which reads

$$\tilde{\sigma}(\omega) = \epsilon_0 + \frac{i\tilde{\sigma}(\omega)}{\omega} \tag{3.13}$$

3.2 Fresnel equations

Since, from the experimental perspective, we are going to measure optical quantities such as the reflectivity and transmissivity, it is interesting to find how they are related to the dielectric function. To do so, we can exploit Fresnel coefficients. To compute these coefficient we have to study separately the boundary conditions for the two cases of light polarization: s-polarization (electric field perpendicular to the plane of incidence) and p-polarization (electric field parallel to the plane of incidence). The two reflectivities read

$$\begin{aligned} R_s = |r_s|^2 &= \left| \frac{n_1 \cos\theta_i - n_2 \cos\theta_t}{n_1 \cos\theta_i + n_2 \cos\theta_t} \right|^2 \\ R_p = |r_p|^2 &= \left| \frac{n_1 \cos\theta_t - n_2 \cos\theta_i}{n_1 \cos\theta_t + n_2 \cos\theta_i} \right|^2 \end{aligned} \tag{3.14}$$

where n_1 is the refracted index of the incident wave medium, n_2 the one on the transmitted side, θ_i the incidence angle and θ_t the transmission angle. We know that the reflected wave angle is equal to the incident one ($\theta_r = \theta_i$) and from Snell's law that the transmitted and incident angles are related by $n_1 \sin\theta_i = n_2 \sin\theta_t$. So we can write the coefficients $R_{s,p}$ depending only on the incidence angle. In the case of non-absorbing medium, $|r_{s,p}|^2 + |t_{s,p}|^2 = 1$, so once we know the reflectivity we can compute the transmissivity.
If we are considering only randomly-polarized light, then the total reflectivity is just the average of the two coefficients:

$$R_{tot} = \frac{1}{2}(R_s + R_p) \tag{3.15}$$

If then we consider normal incidence and the interface between air and a sample ($n_1 \simeq 1$), the formula for reflectivity reads

$$R = \left|\frac{\tilde{n}_2 - 1}{\tilde{n}_2 + 1}\right|^2 = \left|\frac{\sqrt{\tilde{\epsilon}} - 1}{\sqrt{\tilde{\epsilon}} + 1}\right|^2 \tag{3.16}$$

where we have used the fact that $\tilde{n} = \sqrt{\epsilon}$ as seen in eq. 3.7. Thus, it is possible to directly relate reflectivity and transmissivity to the dielectric function.

3.3 Drude Lorenz model

The next brick we need in order to be able to analyse experimental data is a model for the dielectric function. To do so, we can exploit Drude-Lorentz model.
Basically, the main assumptions of the model are the following:

- the atom is described only but two charges with masses M and m (where $M \gg m$), where M represent the nucleus and m the electron,
- there is a elastic recall force acting on the electron,
- there is a damping force felt by the electron due to collisions and radiation emission,
- the electric field gives a driving force.

Moreover, from the definition of polarization vector field

$$\boldsymbol{P} = \lim_{\Delta V \to 0} \frac{\boldsymbol{\Delta p}}{\Delta V} \tag{3.17}$$

we can think that on the average the displacement of the electron with respect to the nucleus leads to an electric dipole, so in general we have that

$$\boldsymbol{P} = Nq\boldsymbol{r} \tag{3.18}$$

where N is the density of atomic dipoles and $q = -e$ the charge of the electron. Following a classical treatment we can write the Newton's law for this system, where the atom position is fixed (due to $M \gg m$):

$$m\frac{d^2\boldsymbol{r}}{dt^2} = -k\boldsymbol{r} - \beta\frac{d\boldsymbol{r}}{dt} - e\boldsymbol{E} \tag{3.19}$$

Now assuming a harmonic electric field $\boldsymbol{E}(t) = \boldsymbol{E}_0 e^{-i\omega t}$ (with a displacement much smaller than the field wavelength), we can look for a solution in the form $\boldsymbol{r}(t) = \boldsymbol{r}_0 e^{-i\omega t}$, which gives, substituting in the previous equation:

$$\begin{aligned} -\omega^2 m\boldsymbol{r}_0 &= -k\boldsymbol{r}_0 + i\omega\beta\boldsymbol{r}_0 - e\boldsymbol{E}_0 \\ -\omega^2\boldsymbol{r}_0 &= -\omega_0^2\boldsymbol{r}_0 + i\omega\gamma\boldsymbol{r}_0 - \frac{e}{m}\boldsymbol{E}_0 \\ \boldsymbol{r}_0 &= \frac{-e}{m}\frac{1}{(\omega_0^2 - \omega^2) - i\gamma\omega}\boldsymbol{E}_0 \end{aligned} \tag{3.20}$$

where ω_0 is the resonance frequency and $\gamma = \beta/m$.
From the constitutive relations, we know that $\boldsymbol{P} = \epsilon_0(\epsilon(\omega) - 1)\boldsymbol{E}$ and with 3.18 we can now write

$$\begin{aligned} \epsilon(\omega) - 1 &= \frac{-eN}{m\epsilon_0}\frac{1}{(\omega_0^2 - \omega^2) - i\gamma\omega} \\ \epsilon(\omega) &= 1 + \frac{\omega_p^2}{(\omega_0^2 - \omega^2) - i\gamma\omega} = \\ 1 + \frac{\omega_p^2(\omega_0^2 - \omega^2)}{(\omega_0^2 - \omega^2)^2 + \gamma^2\omega^2} &+ i\frac{\omega_p^2\gamma\omega}{(\omega_0^2 - \omega^2)^2 + \gamma^2\omega^2} \end{aligned} \tag{3.21}$$

where $\omega_p = \sqrt{\frac{Ne^2}{\epsilon_0 m}}$ is the plasma frequency. We can improve this general Drude-Lorentz model if we consider that we have n bound electrons which are responsible for the material behaviour and if we take into account also the high-frequency limit for the dielectric function (ϵ_∞). The dielectric function reads

$$\epsilon(\omega) = \epsilon_\infty + \sum_{i=1}^{n}\frac{\omega_{p,i}^2(\omega_{0,i}^2 - \omega^2)}{(\omega_{0,i}^2 - \omega^2)^2 + \gamma_i^2\omega^2} + i\sum_{i=1}^{n}\frac{\omega_{p,i}^2\gamma_i\omega}{(\omega_{0,i}^2 - \omega^2)^2 + \gamma_i^2\omega^2} \tag{3.22}$$

where we clearly see the real and imaginary parts of the dielectric function. In metals, free electrons do not feel the restoring force and can freely move among the atoms. Thus, in the case of metallic samples, we need to consider also an oscillator with $\omega_0 = 0$, which gives the so-called *Drude term.*

3.4 Kramers-Kronig relations and sum rules

In the framework of linear response theory we can generally write

$$\hat{X}(\boldsymbol{r}, t) = \iint_{-\infty}^{\infty}\hat{G}(\boldsymbol{r}, \boldsymbol{r}', t, t')\hat{f}(\boldsymbol{r}', t')d\boldsymbol{r}'dt' \tag{3.23}$$

where $\hat{X}$ represents the response of the system at coordinate $\boldsymbol{r}$ at time t, $\hat{G}$ is the response function and $\hat{f}$ represents the stimulus. For instance, the dielectric function or the conductivity can be considered as response function since, in the first case, we can write

$$\boldsymbol{P}(\boldsymbol{r},t) = \epsilon_0 \iint_{-\infty}^{\infty} (\hat{\tilde{\epsilon}}(\boldsymbol{r},\boldsymbol{r}',t,t') - 1)\boldsymbol{E}(\boldsymbol{r}',t')d\boldsymbol{r}'dt' \tag{3.24}$$

Now let us assume that the response function is a local function and the time dependence is only on the difference $t - t'$ (the time scale origin is not important):

$$\hat{G}(\boldsymbol{r},\boldsymbol{r}',t,t') = \delta(\boldsymbol{r}-\boldsymbol{r}')\hat{G}(t-t') \tag{3.25}$$

Moreover we do the same assumptions as in eq. 3.5, i.e. that the medium is isotropic and homogeneous (scalar response function), then we find:

$$\hat{X}(t) = \int_{-\infty}^{\infty} \hat{G}(t-t')\hat{f}(t')dt' = \hat{G}(t) * \hat{f}(t) \tag{3.26}$$

In Fourier domain, the convolution transforms into a simple product

$$\hat{X}(\omega) = \hat{G}(\omega) * \hat{f}(\omega) \tag{3.27}$$

For mathematical reasons, let us assume a complex frequency $\tilde{\omega} = \omega_1 + i\omega_2$, so the response function becomes

$$\hat{G}(\tilde{\omega}) = \int \hat{G}(t-t')e^{i\omega_1(t-t')}e^{-\omega_2(t-t')}dt \tag{3.28}$$

and in order to have causality[1] we restrict to the upper half-plane for $t-t' > 0$ where the exponential factor is bounded.
The Fourier transform of the response function is called frequency dependent generalized susceptibility, where the real part describes the attenuation of the stimulus, while the imaginary part is responsible of the phase difference between the response of the system and the external perturbation. From a mathematical point of view, since the function is analytic in the upper-half plane, Cauchy theorem holds and we have that

$$\oint_\gamma \frac{\hat{G}(\tilde{\omega}')}{\tilde{\omega}' - \tilde{\omega}_0} d\tilde{\omega}' = 0 \tag{3.29}$$

where γ is the closed contour of the upper half plane, as represented in figure 3.1.
When we perform the integral on the large semicircle we see that when $\tilde{\omega} \to \infty$, $\hat{G}(\tilde{\omega}) \to 0$, so this contribution vanishes. This means that

$$\oint_\gamma \frac{\hat{G}(\tilde{\omega}')}{\tilde{\omega}' - \tilde{\omega}_0} d\tilde{\omega}' = \int_c \frac{\hat{G}(\tilde{\omega}')}{\tilde{\omega}' - \tilde{\omega}_0} d\tilde{\omega}' \tag{3.30}$$

[1] In fact, we need that $\hat{G}(t-t') = 0$ if $t < t'$.

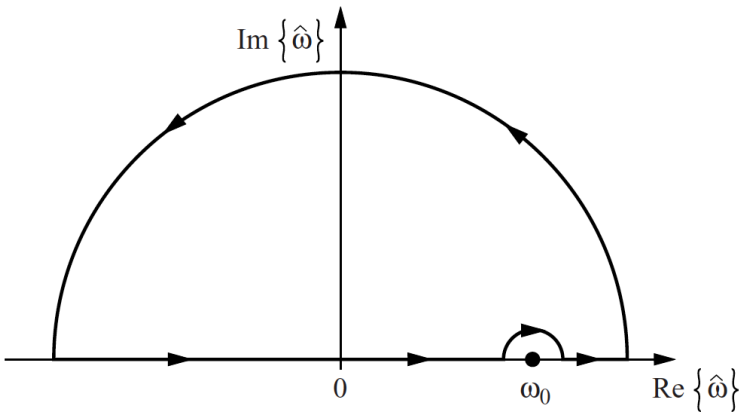

Figure 3.1: Integration contour in the frequency complex plane.

where c represents the small semicircle around $\tilde{\omega}_0$ of radius η. From complex analysis theorems, we know that we can compute this integral in the limit $\eta \to 0$ and we find

$$\lim_{\eta \to 0} \int_{\tilde{\omega}_0 - \eta}^{\tilde{\omega}_0 + \eta} \frac{\hat{G}(\tilde{\omega}')}{\tilde{\omega}' - \tilde{\omega}_0} d\tilde{\omega}' = -i\pi \hat{G}(\tilde{\omega}_0) \tag{3.31}$$

which is equivalent to write

$$\hat{G}(\tilde{\omega}) = \frac{1}{i\pi} \mathcal{P} \int_{-\infty}^{\infty} \frac{\hat{G}(\tilde{\omega}')}{\tilde{\omega}' - \tilde{\omega}} d\tilde{\omega}' \tag{3.32}$$

This means that writing $\hat{G}(\omega) = G_1(\omega) + iG_2(\omega)$, we find

$$\begin{aligned} G_1(\omega) &= \frac{1}{\pi} \mathcal{P} \int_{-\infty}^{\infty} \frac{G_2(\omega')}{\omega' - \omega} d\omega' \\ G_2(\omega) &= -\frac{1}{\pi} \mathcal{P} \int_{-\infty}^{\infty} \frac{G_1(\omega')}{\omega' - \omega} d\omega' \end{aligned} \tag{3.33}$$

which are the Kramers-Kronig relations. $G_1(\omega)$ and $G_2(\omega)$ can be seen as the Hilbert transforms of each other.

3.4.1 Optical Kramers-Kronig relations

For example, if we consider the conductivity, which links the current density to the electric field, we can write the following relations:

$$\begin{aligned} \sigma_1(\omega) &= \frac{1}{\pi} \mathcal{P} \int_{-\infty}^{\infty} \frac{\sigma_2(\omega')}{\omega' - \omega} d\omega' \\ \sigma_2(\omega) &= -\frac{1}{\pi} \mathcal{P} \int_{-\infty}^{\infty} \frac{\sigma_1(\omega')}{\omega' - \omega} d\omega' \end{aligned} \tag{3.34}$$

but in this case negative frequencies have no physical meaning, so let us change a bit the shape of this integral[2]. We know that $\hat{\sigma}^*(\omega) = \hat{\sigma}(-\omega)$ (i.e. $\sigma_1(\omega) = \sigma_1(-\omega)$ and $\sigma_2(-\omega) = -\sigma_2(\omega)$) and so we can derive Kramers-Kronig relation for conductivity

$$\begin{aligned} \sigma_1(\omega) &= \frac{2}{\pi}\int_0^{+\infty} \frac{\omega'\sigma_2(\omega')}{\omega'^2 - \omega^2} d\omega' \\ \sigma_2(\omega) &= -\frac{2\omega}{\pi}\int_0^{+\infty} \frac{\sigma_1(\omega')}{\omega'^2 - \omega^2} d\omega' \end{aligned} \tag{3.36}$$

Let us do the same for the dielectric constant, which relates the electric field to the polarization field. Remembering the relations 3.12 and 3.10, we write

$$\begin{aligned} \epsilon_2(\omega) &= -\frac{2}{\pi\omega}\int_0^{+\infty} \frac{\omega'^2(1 - \epsilon_1(\omega'))}{\omega'^2 - \omega^2} d\omega' \\ \epsilon_1(\omega) &= 1 + \frac{2}{\pi}\int_0^{+\infty} \frac{\omega\epsilon_2(\omega')}{\omega'^2 - \omega^2} d\omega' \end{aligned} \tag{3.37}$$

Analogously there are Kramers-Kronig relations also between the reflectivity (R) and the phase (ϕ). In the analysis in chapter 6, the relation which maps the reflectivity into the phase reads:

$$\phi_r(\omega) = \frac{\omega}{\pi}\int_0^{\infty} \frac{\ln R(\tilde{\omega}) - \ln R(\omega)}{\omega^2 - \tilde{\omega}^2} d\tilde{\omega} \tag{3.38}$$

Once the phase as a function of frequency is known, it is possible to compute the complex dielectric function and the optical conductivity, which reads:

$$\begin{cases} \sigma_1(\omega) = \omega\epsilon_0 \frac{4\sqrt{R(\omega)}[1-R(\omega)]\sin\phi_r(\omega)}{\left[1+R(\omega)-2\sqrt{R(\omega)}\cos\phi_r(\omega)\right]^2} \\ \sigma_2(\omega) = -\omega\epsilon_0\left(1 - \frac{4\sqrt{R(\omega)}-4R(\omega)\sin^2\phi_r(\omega)}{\left[1+R(\omega)-2\sqrt{R(\omega)}\cos\phi_r(\omega)\right]^2}\right) \end{cases} \tag{3.39}$$

3.4.2 Sum rules

If we consider the last integral expression for ϵ_1 in eq. 3.37, when ω is large, we can write

$$\epsilon_1(\omega) \simeq 1 - \frac{2}{\pi\omega^2}\int_0^{\infty} \omega'\epsilon_2(\omega')d\omega' \tag{3.40}$$

[2]In general for a function f, exploiting the properties of odd and even functions, the following holds

$$\mathcal{P}\int_{-\infty}^{\infty} \frac{f(x)}{x-a}dx = \mathcal{P}\int_0^{\infty} \frac{x(f(x)-f(-x)) + a(f(x)+f(-x))}{x^2-a^2}dx \tag{3.35}$$

If we take the Drude-Lorentz model for a single oscillator we see that for large ω ($\omega \gg \omega_o, \gamma$),

$$\epsilon_1 \simeq 1 + \frac{\omega_p^2}{\omega^2} \tag{3.41}$$

and substituting in the previous equation, we find

$$\frac{\pi\omega_p^2}{2} = \int_0^\infty \omega\epsilon_2(\omega)d\omega \tag{3.42}$$

Expressing it in terms of conductivity, it reads

$$\frac{\pi\epsilon_0\omega_p^2}{2} = \int_0^\infty \sigma_1(\omega)d\omega = \frac{\pi N e^2}{2m} \tag{3.43}$$

Moreover, it can be shown that for n oscillators, the sum rules reads

$$\int_0^\infty \sigma_1(\omega)d\omega = \frac{2}{\pi}\sum_i^n \frac{q_i^2}{m_i} \tag{3.44}$$

3.5 RefFit

In this section the software used to fit the analytical model to experimental data will be discussed.
Reffit is a user-friendly software developed by A. Kuzmenko, where it is possible to model the sample and its optical response. Furthermore, an automatic fit is implemented for the optical quantities. With Reffit, it is possible to fit simultaneously many optical quantities, fix restraints, and give different weights to different quantities.
There are many models for the dielectric function which can be used in Reffit: Drude-Lorentz model, Fano-shaped Lorentz model and many others which apply to specific materials.
In Reffit two forms of the so-called variational dielectric function (VDF) are also implemented: the Kramers-Kronig constrained and the not KK-constrained one. In the not-KK-constrained regime the real and imaginary parts (ϵ_1 and ϵ_2) of the dielectric function are treated as independently varied parameters, while in the KK regime the varied parameter is only ϵ_2 and ϵ_1 is computed with Kramers-Kronig transformation. The VDF method allows to easily fit, for instance, reflectivity and find the optical conductivity.

3.6 FT-IR spectroscopy

As discussed in the previous sections, to gain information on optical conductivity of the material, we have to perform experiments to measure, for instance, reflectivity or transmissivity . In this project, the focus is Fourier-Transform InfraRed (FT-IR) spectroscopy.

The main idea is to measure the reflectivity of the sample in function on the energy of the impinging light. Thus we measure reflectivity spectrum (from this the word *spectroscopy*).
Since we want to study the temperature-dependent behaviour of the phonons, we need to consider energy of the same magnitude. This means we have to use a radiation whose energy is roughly between a few meV and one eV. In the field of optical spectroscopy, the usual quantity is wavenumber (cm^{-1}). The relation with electronvolt is simply given by

$$\begin{aligned} E = \hbar\omega = \hbar ck = \hbar c \frac{2\pi}{\lambda} \\ E[\mathrm{meV}] = 0.12398 E[\mathrm{cm}^{-1}] \end{aligned} \tag{3.45}$$

The aforementioned range is the one of infrared (IR) radiation, which can can be subdivided it into three different regions:

- FIR (Far InfraRed), between $10\mathrm{cm}^{-1}$ and $650\mathrm{cm}^{-1}$,
- MIR (Middle InfraRed), between $650\mathrm{cm}^{-1}$ and $7000\mathrm{cm}^{-1}$,
- NIR (Near InfraRed), above $7000\mathrm{cm}^{-1}$ up to visible light.

To obtain the spectra, i.e., the wavenumber-dependent optical quantities, we need to perform a Fourier transform of the measured signal. This is the work done by the spectrometer, which will be explained in the following section.

CHAPTER 4

Experimental setups

As discussed in the previous chapter, information on the optical conductivity of the material can be gained from optical spectroscopy experiments.
In this work, the focus lies on FT-IR (Fourier-transform infrared) spectroscopy which allowed to measure the following quantities:

- Reflectivity in FIR and MIR region (for $SrTiO_3$ and $Ca_xSr_{1-x}TiO_{3-\delta}$)
- MIR Transmissivity (only for $SrTiO_3$)
- THz transmissivity (only for $SrTiO_3$)

In this section, the working principles of the experimental setups will explained and the measurements procedures will be described.

4.1 Spectrometer

Let us start from the main part of the experimental setup: the spectrometer. In this project, different commercial spectrometers were used, in particular:

- Bruker IFS 113v spectrometer for the reflectivity in the FIR region,
- Bruker VERTEX 70v spectrometer with a HYPERION microscope for the reflectivity in the MIR region,
- Bruker IFS 66 V/s spectrometer for the transmissivity and reflectivity measurements in the MIR region.

The main working principle is the same in the different spectrometers and it is illustrated in figure 4.2.

(a) Bruker IFS 113v.

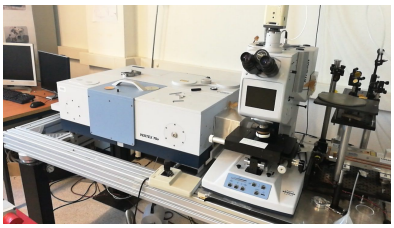

(b) Bruker Vertex 70v with microscope.

Figure 4.1: FT-IR spectrometers used for reflectivity measurements.

Since the goal is to perform a Fourier transform on the measured signal, it is necessary to gain information in the frequency domain. To do so, a Michelson-Morley interferometer can be exploited: the beamsplitter divides the light coming from the IR source (with a broad spectrum) into two beams, one returns directly on the beamsplitter after the reflection on a fixed mirror, while the other one is reflected by a moving mirror, whose position is measured by a laser. Due to the continuous movement of the mirror, destructive interference cuts some components (at given frequencies) of the IR radiation. The resulting beam impinges on the sample with (almost) normal incidence and the detector measures the intensity.
From the intensity measured as a function of the position of the mirror, the so-called interferogram, it is possible to calculate the spectrum of the signal

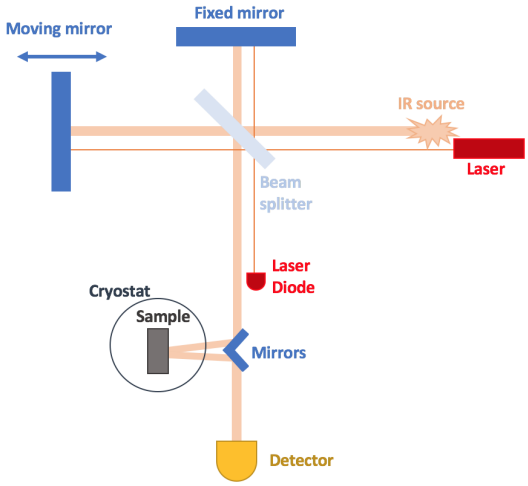

Figure 4.2: FTIR spectrometer working scheme.

by using Fourier transformation.
To be precise, the sliding mirror is only present in the IFS 113v, while in the other spectrometer Bruker has implemented a different interferometer system: RockSolid^{TM}. It exploits dual retro-reflecting cube corner mirrors in an inverted double pendulum arrangement with a pivot mechanism at the centre of mass, which leads to a periodic, continuous change of the optical path[1].
When a measurement is taken, it is really important to measure only the light reflected by the sample and not the sample-holder. To achieve this, the focus of the beam lies in the sample plane. Furthermore, the sample-holder has a conic shape, so that some light impinging on it is reflected away from the detector.
Moreover, it is possible to change the beam size by selecting different apertures: inside the interferometer, just after the sources, there is a disc (with holes of different diameters) which can rotate in order to set the size of the outgoing beam.
The spectrometers work under vacuum at pressures around 5mbar to avoid air absorption peaks.

4.1.1 Sources and beamsplitter

As seen above, it is necessary to have light sources providing different energy spectra to measure the complete reflectivity spectrum. In our measurements the following light sources were used:

- Mercury lamp for FIR region
- Globar lamp for MIR region

The sources have to be stable during the measurements.

Another crucial part of the interferometer is the beamsplitter. In fact it intrinsically selects a range of frequencies which are well-transmitted. Thus, for every different sources and depending on the measured range, there is a suitable beamsplitter. In this project the following beamsplitters were used:

- KBr covered by a thin layer of Ge for the MIR range,
- Mylar6µm (a bi-axially oriented polyester film) for the FIR range,
- Si10 for the FIR region below 100cm^{-1}.

[1]The system is thus immune to errors due to mirror tilt, which would lead to worse resolution and lower spectral quality.

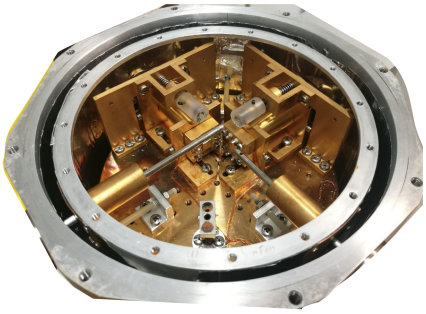

(a) Bolometer detector interior.

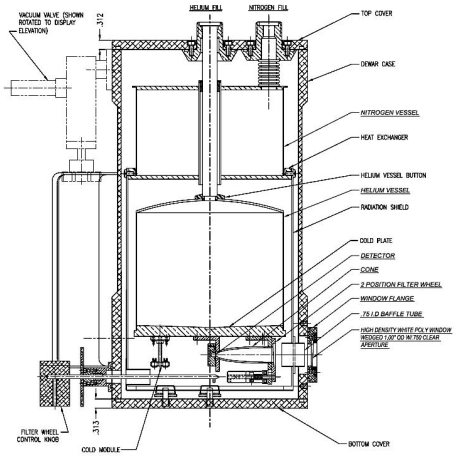

(b) Bolometer scheme[2].

Figure 4.3: IRLabs bolometer used for FIR measurements.

4.2 Detectors

To measure a complete spectrum, data from three different energy ranges have to be merged and in order to have the best signal in each interval, different detectors with different working principles were used.

4.2.1 Bolometers 1.6 and 4.2 K

The reflectivity in the FIR region was measured with bolometers. The working principle of a bolometer is to measure the heat induced by the impinging infrared radiation. Because of this ,the thermal noise has to be filtered out by cooling the detector down to liquid He temperature.
In this work, bolometers from IRLabs, with a high purity N-type InSb crystal (cooled down to 4.2K) as detector element, were used. At low temperature the absorption of radiation by free electrons leads to an increase of the average temperature of the electrons (T_0). Since electron mobility is proportional to $T^{\frac{3}{2}}$, it is possible to measure the temperature change as a change in conductivity. The working temperature of the bolometer depends on the desired energy range. In this work the following were used:

- 1.6 K (pumping on liquid helium) for FIR from 10cm^{-1} to 100cm^{-1},
- 4.2 K (liquid helium) for FIR from 100cm^{-1} to 800cm^{-1}.

Figure 4.3b shows a scheme of the bolometer: a pumped external casing ($p \simeq 4 \times 10^{-6}$mbar) contains the liquid nitrogen vessel and the liquid helium

[2]From http://www.infraredlaboratories.com/uploads/Basic_Bolometer_DWG.jpg

vessel; the former one is used as a pre-cooler to avoid a fast evaporation of liquid He. The real detector, with light entrance and a golden conical mirror to better focus it, is attached to the bottom of the liquid He vessel. These structures are mechanically decoupled from the external casing through a spring, in order to avoid any mechanical vibrations, which can increase the noise.
Figure 4.3a shows a picture of the interior of the bolometer, where the two detectors for the two working temperatures can be distinguished.

Bolometers can have high resolution and precision also for low wavenumbers, but on the other hand the limiting factor is the bandwidth: we measure change of resistivity so it is necessary to wait for the detector to go back to its initial state. This is why pulsed sources are needed and not continuous light.

4.2.2 MCT

For the MIR energy region, MCT (HgCdTe) detectors can be used instead of bolometers. HgCdTe is a semiconducting material whose gap can be tuned by changing the concentration of the two components of the alloy: CdTe and HgTe.
Once the detector is cooled down to liquid nitrogen temperature (77K), it is possible to reduce the noise due to thermally-excited carriers and use it for FT-IR measurements. An important advantage with respect to bolometers is the large bandwidth, in fact it exploits Auger processes, much faster than heat conduction as in the case of bolometers.

4.3 Cryostat and gold evaporator

In order to do temperature-dependent measurements, two different liquid-He flow cryostats (shown in figure 4.4) were used: one adapted to the Bruker IFS 113v and the other one to the microscope setup. Let us consider separately the two systems used to measure reflectivity.
In the Bruker IFS 113v, the cryostat can cool down to a minimum temperature of around 9 K and a turbo pump provides a pressure around 10^{-7}mbar. Inside the cryostat there is a gold evaporator which allows to evaporate a thin Au layer in-situ on top of the sample so that the reference spectrum can be measured without taking out the sample.
In the case of the microscope system, there is no gold evaporator inside the cryostat so an Au reference is evaporated on part of the sample before mounting it in the cryostat.

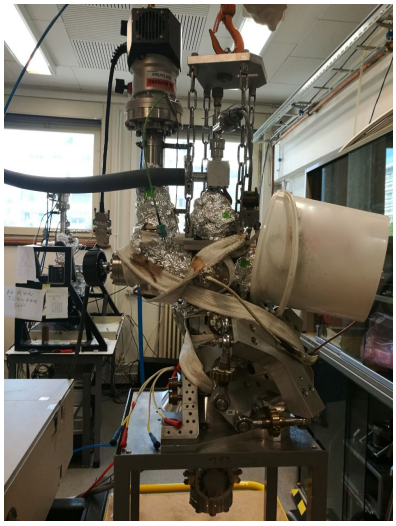

(a) Cryostat for IFS 113v

(b) Cryostat for microscope interferometer

Figure 4.4: Cryostats used for reflectivity measurements.

4.4 Measurement procedure

First of all, in order to have consistent and comparable data, a precise sample preparation and measurement procedure has been established, based on $SrTiO_3$ measurements.
During the first measurements at room temperature, a large value of reflectivity above 800 cm^{-1} was observed: it was due to the reflection from the back side of the sample. In fact in this region the transmissivity of pure STO is around 80%, which means that the impinging light is also reflected by the back side of the sample. In order to avoid this effect different options have been tried:

- unpolished back side,
- black paint on the back side,
- black scotch on the back side,
- focusing the beam on the upper face using the spectrometer with the microscope.

As represented in figure 4.5, the correct signal[3] is given by the last technique (with the microscope system) combined with unpolished back surface. All the measurements of MIR region reflectivity were taken with this technique.

[3]We compare the results to previous reflectivity data [40] [41].

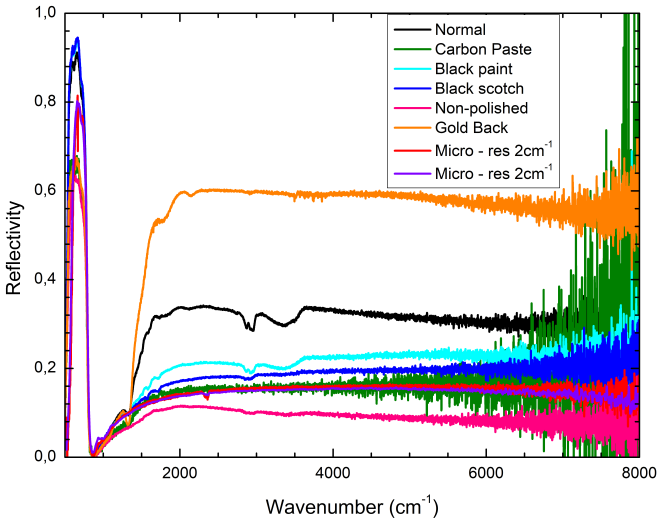

Figure 4.5: Comparison of MIR reflectivity spectra between different techniques for $SrTiO_3$ sample at 300 K.

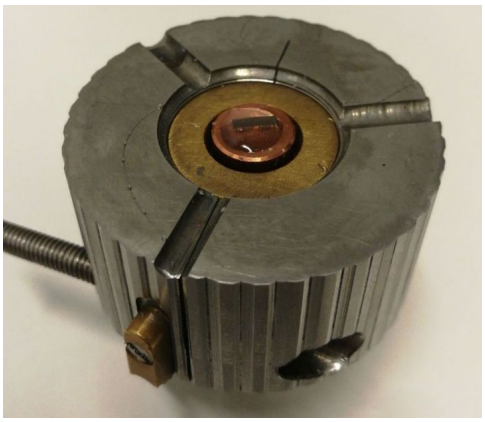

Figure 4.6: Polishing support

Since the Ca-substituted STO samples were unpolished and reflectivity data are very sensible of the polishing quality, polishing was carefully done, using the support showed in figure 4.6. The quality was quantified by looking at the reflected spot of the laser used to align the sample once glued on the sample-holder. In case of a bad polishing, the reflected spot is blurry and wide, while for a good polishing the spot is more well-defined and net.
The following procedure was established for Bruker IFS 113v:

- Measurement of the sample reflection spectrum

- Temperature dependent measurements of the sample reflectivity from room temperature down to 9 K,
- Temperature ramp back to the initial temperature K (no measurements),
- Measurement of the sample reflectivity spectrum and comparison with initial spectrum to check the stability of the system,
- Gold evaporation,
- Measurement of the reference gold reflection spectrum,
- Temperature dependent measurements of the gold surface reflectivity from room temperature down to 9 K
- Temperature ramp back to the initial temperature K (no measurements).

Once the spectra for both the sample and the gold are measured, by computing their ratio

$$\text{Reflectivity} = \frac{\text{Sample spectrum}}{\text{Gold spectrum}} \tag{4.1}$$

the reflectivity spectrum of the material can be found.

4.5 THz transmissivity

THz transmissivity measurements were done using the TeraView TPS Spectra 3000 spectrometer.
As in FTIR spectroscopy, the sample chamber is pumped and evacuated from nitrogen and air (to avoid their absorption). But in this case, the technique is called THz Time-Domain Spectroscopy because it is based on a fast electromagnetic pulse (with picosecond duration) which is then transmitted through the sample and measured by the detector as a function of time. Once the sample and the reference electric fields are measured, computing their FFT and taking the ratio, it is possible to find the transmissivity.

$$T = \left| \frac{\mathcal{F}\left[E_{\text{sample}}\right]}{\mathcal{F}\left[E_{\text{reference}}\right]} \right|^2 \tag{4.2}$$

The reference signal is the electric field when the electromagnetic radiation is transmitted through the bare hole. The power of THz TDS is that Kramers-Kronig relations are not necessary (but they can be used to check causality and quality of data), since instead of intensity, the detector measure the transmitted electric field. Thus the Fourier transform of it gives both the real and imaginary parts.

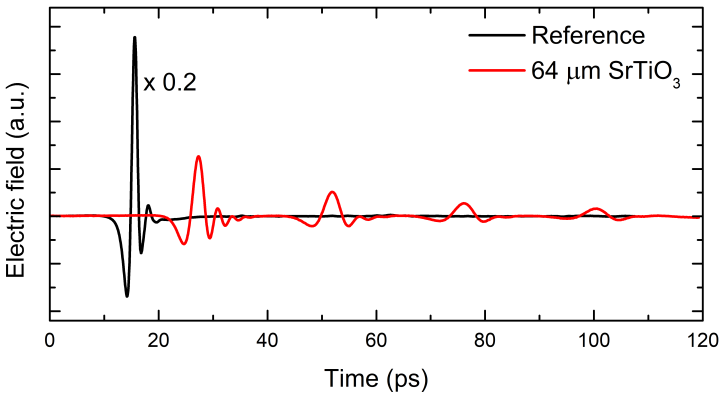

Figure 4.7: THz time-resolved electric field for sample and reference.

4.6 Raman spectroscopy

Raman measurements were taken using LabRam HR Evolution Horiba.

The Raman technique is complementary to FT-IR spectroscopy since it allows to measure modes which can be IR inactive. A mode is Raman active if the electric dipole polarizability derivative is non zero, while it is IR active if it presents a non-zero electric dipole moment derivative.

The basic principle of the Raman technique is the following: a monochromatic laser impinges on the sample and it is reflected back to the detector. The reflected light consists of a huge elastic peak (at the same energy of the source) and the Raman-scattered part, which can have different frequency components. If one thinks of the phonons as a set of discrete vibrational levels, then the impinging light (of energy $h\nu$) can excite the system from its state to a virtual one and when it relaxes back, the system could go to a different vibrational level. If the new level has higher energy than the initial one, then the detected signal has a smaller frequency. In fact, the energy conservation law gives:

$$h\nu_0 = h\nu_d \pm \hbar\omega \tag{4.3}$$

where ν_0 is the frequency of the source, ν_d is the frequency of the detected photon and ω is the frequency of the excitation, for instance of a phonon.
In the case of a negative sign, i.e., a negative $\Delta\nu = \nu_0 - \nu_d$, the resulting peaks are called anti-Stokes peaks, while if $\Delta\nu$ is positive, they are Stokes peaks. In the case of a Stokes process, the final state has a higher energy than the initial state, which means that one phonon has been excited.
Thus, with Raman spectroscopy it is possible to measure the hardening of the soft ferroelectric mode in Ca-substituted strontium titanate.

CHAPTER 5

Experimental Measurements

The samples reported in table 5.1, used for previous studies [25], were measured.

Figure 5.1 shows the Curie temperatures (T_C) of the ferroelectric samples

Material	Ca concentration x	Carrier concentration [cm^{-3}]	Thickness [µm]
$SrTiO_3$	-	-	500
$SrTiO_3$	-	-	64
$Ca_xSr_{1-x}TiO_3$	0.0022	-	800
$Ca_xSr_{1-x}TiO_3$	0.0045	-	500
$Ca_xSr_{1-x}TiO_{3-\delta}$	0.0045	9.2×10^{17}	500
$Ca_xSr_{1-x}TiO_{3-\delta}$	0.0045	5×10^{18}	500
$Ca_xSr_{1-x}TiO_{3-\delta}$	0.0045	10^{19}	500

Table 5.1: Overview of the measured $SrTiO_3$ and $Ca_xSr_{1-x}TiO_{3-\delta}$ samples.

and the anomaly temperature, i.e., the temperature at which the ferroelectric-like order is measured, which can be considered analogous to T_C for the insulating samples.

For all the samples, temperature dependent reflectivity spectra were measured. Moreover, MIR transmissivity and THz transmissivity of the 64µm-thick $SrTiO_3$ sample were measured.

The transport properties, in particular the DC conductivity (σ_{DC}) and the carrier concentration, of the n-doped samples were measured previously [25].

In the first part of this chapter, experimental data about $SrTiO_3$ are presented, i.e. reflectivity, MIR transmissivity and THz transmissivity spec-

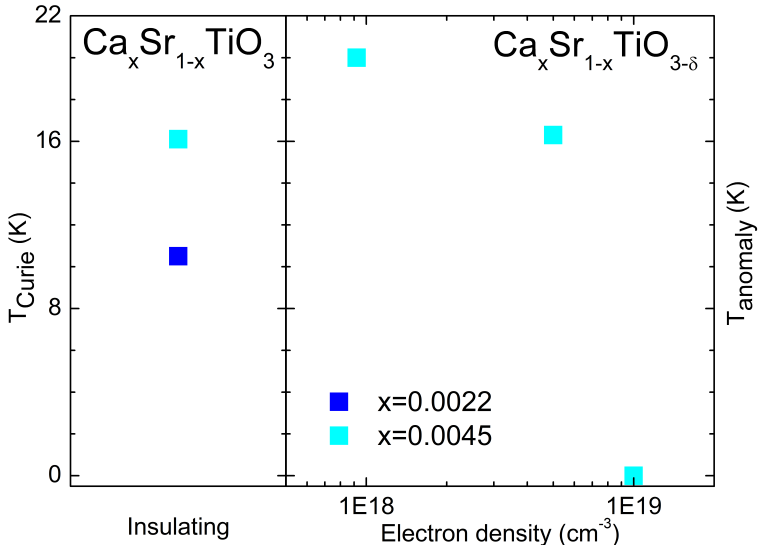

Figure 5.1: Curie temperature T_{Curie} and anomaly temperature for $Ca_xSr_{1-x}TiO_{3-\delta}$ samples.

tra. In the second part, measurements of Ca-substituted and n-doped STO samples are shown.

5.1 $SrTiO_3$ spectroscopy

5.1.1 Temperature dependence of reflectivity

Figure 5.2 shows the reflectivity spectra of STO at two different temperatures: 10 and 300 K.

From the experimental spectra we can already try to identify the phonons. Let us first discuss the spectrum at room temperature. Around 90cm^{-1} the TO1 mode can be found, which corresponds to the vibration of Ti cations against the oxygen octahedra, as illustrated in figure 5.3a. This is the so-called *soft mode*, related to the ferroelectric transition. At 180cm^{-1} the TO2 phonon is found, which is related to the vibrations of Sr against TiO_6 octahedra, as represented in figure 5.3b.
The last phonon which can be seen in the spectrum is the TO4 mode around 500cm^{-1} which represents the bending of oxygen octahedra, shown in 5.3c. Eventually, at 800cm^{-1} a sharp plasma edge is present.

Now, let us look at the low temperature spectrum measured at 10 K. The reflectivity increases for wavenumbers smaller than the plasma edge and also an excitation peak related to the AFD transition appears below

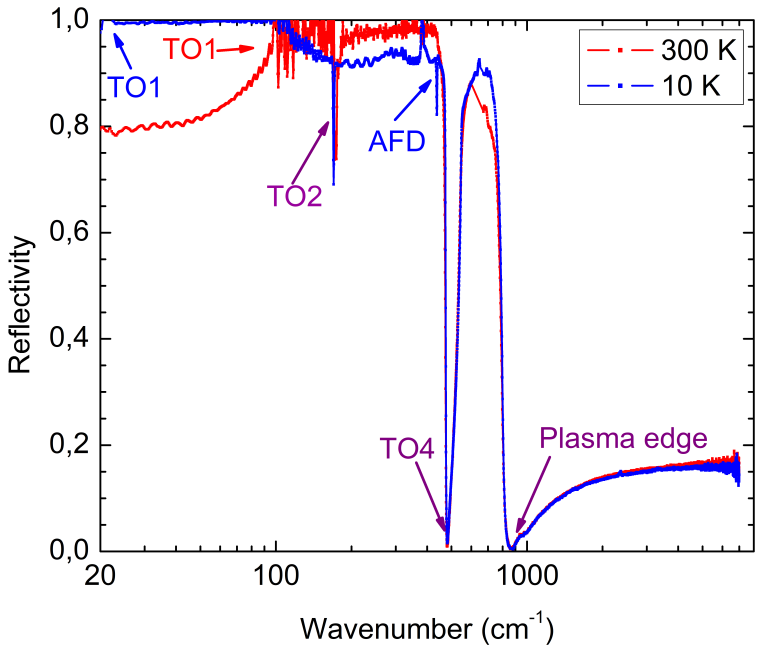

Figure 5.2: Reflectivity spectra of $SrTiO_3$ at 10 (blue) and 300 K (red).

105 K, around 440cm^{-1}: in fact below this temperature, the material undergoes a structural transition from cubic to tetragonal. The mode we measure corresponds to the rotation of oxygen atoms as represented in figure 5.3d. But the most important effect is the softening of the ferroelectric TO1 phonon, whose frequency is around the measurement limit of the system (20cm^{-1}).

In the next chapter a precise temperature dependent phonon analysis will be presented.

5.1.2 THz transmissivity and MIR transmissivity

As seen from reflectivity spectrum of STO in figure 5.2, in the region up to 800cm^{-1}, the reflectivity is around 80% whereas above the plasma edge it is below 20%. Because of this, the transmissivity in MIR region was measured. Due to the fact that the cryostats of the Bruker spectrometers work only in the reflection configuration, the analysis is restricted to room temperature (300 K).
The second region where transmissivity was measured is the THz region (up to 50cm^{-1}). As explained in the previous chapter, for these measurements a

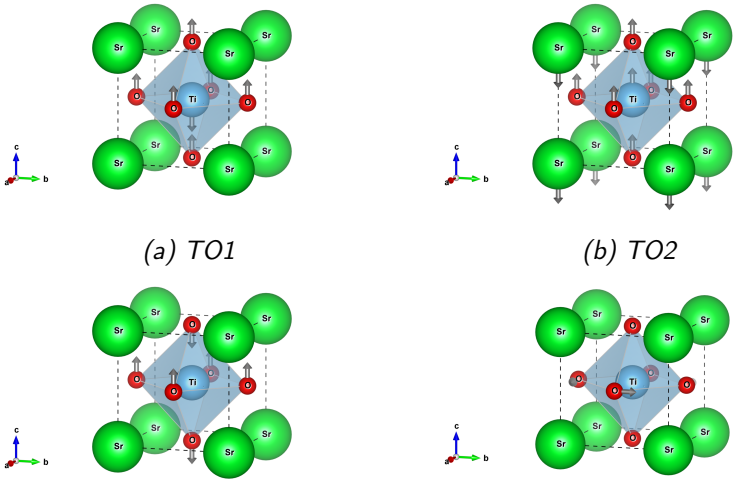

(a) TO1 (b) TO2

(c) TO4 (d) AFD

Figure 5.3: IR-active modes of $SrTiO_3$.

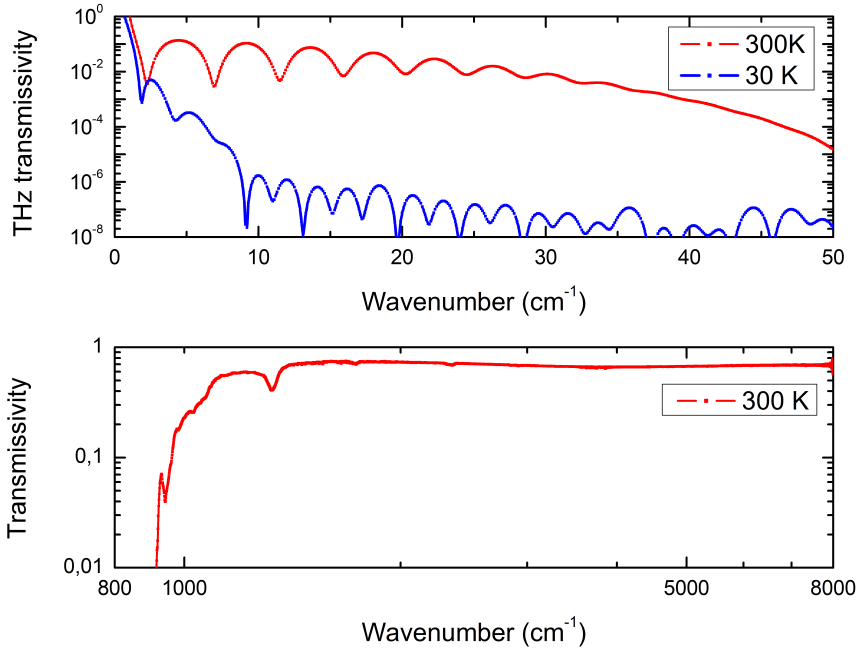

Figure 5.4: Upper panel: $SrTiO_3$ THz transmissivity. Lower panel: $SrTiO_3$ MIR transmissivity.

different setup (the Teraview system) was used, where it is possible to carry out a temperature scan using a flow cryostat. Since the energy range extends up to 50cm^{-1}, it is possible to observe the softening of the ferroelectric soft mode.
In order to obtain the best signal, for these measurements a thinner sample was used (thickness of 64µm).
In figure 5.4, the lower panel shows MIR transmissivity of pure STO at 300 K. It is possible to observe a small absorption at 1400cm^{-1}, which can be identified as a bi-phonon, in agreement with its small strength. The spectrum is in agreement with reflectivity data and also with previous data [41].
In the upper panel of the figure 5.4, THz transmissivity spectra are shown and at low temperature the soft mode is responsible for the low value of transmissivity at higher wavenumbers. Fabry-Pérot fringes due to the thickness of the sample are also visible.
In the following chapter, transmissivity and reflectivity spectra are used simultaneously to find a better fit for the complex dielectric function (using Reffit).

5.2 $Ca_xSr_{1-x}TiO_{3-\delta}$ optical spectroscopy: reflectivity spectra

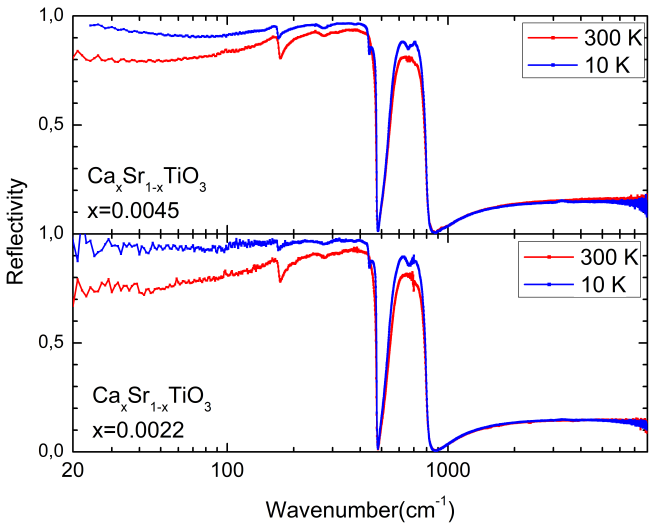

Figure 5.5: Reflectivity spectra at 10 (blue) and 300 K (red) of $Ca_xSr_{1-x}TiO_3$ for Ca concentrations $x = 0.0022$ and $x = 0.0045$.

In this section, reflectivity spectra for Ca-substituted STO are shown. Transmissivity data are not available due to the thickness of samples.

In figure 5.5, reflectivity spectra are presented for insulating samples with Ca concentration of 0.22% (lower panel) and 0.45% (upper panel).
Let us start from room temperature spectra. In both cases the reflectivity spectra show a different behaviour from STO reflectivity. There is not the sharp increase at 100cm^{-1} which means that the TO1 mode has shifted. This is reasonable since some of Sr cations are replaced by Ca, which has a different mass. Moreover, a highly asymmetric TO2 mode is visible at 180cm^{-1}, the asymmetry can be explained by the anisotropic substitution of Ca: we lose the translational symmetry of a perfect crystal. The same considerations stand for the low temperature spectra of the insulating samples, where AFD mode can be found as a sign of the structural antiferrodistortive transition. In both spectra, Fabry-Pérot fringes due to the diamond window of the cryostat appear.

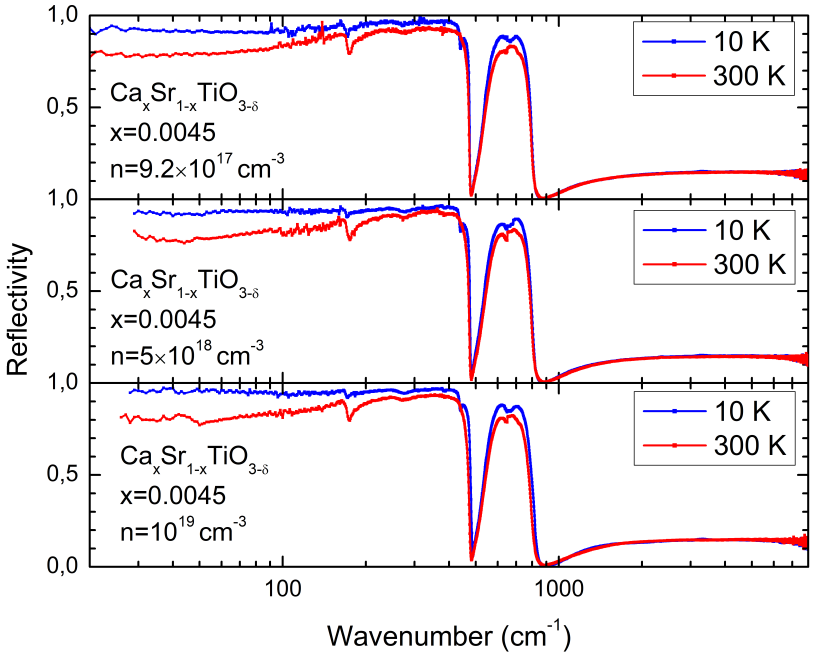

Figure 5.6: Reflectivity spectra of metallic $Ca_xSr_{1-x}TiO_{3-\delta}$, for $x = 0.0045$ and $n = 9.2 \times 10^{17}, 5 \times 10^{18}, 10^{19}\text{cm}^{-3}$.

Let us now consider reflectivity spectra of samples where oxygen is removed (n-doping), i.e. $Ca_xSr_{1-x}TiO_{3-\delta}$ with $x = 0.45\%$.
Since these are metallic samples, Drude peaks are expected to show in their reflectivity spectra and, indeed, it is possible to spot a slight upturn for low wavenumbers. The other phonons stay at the same frequency as in the in-

sulating samples. Qualitatively, it is possible to observe that these spectra are more noisy than the previous ones: it can be due to the smaller size of the samples and thus to lower total number of counts on the detector.

5.3 Raman measurements

Raman measurements were done to identify the TO1 mode in the ferroelectric phase and its temperature dependence, thus adding a complementary information to FTIR reflectivity measurements.

In figure 5.7, the experimental data of $Ca_xSr_{1-x}TiO_{3-\delta}$ (for $x = 0.0045$

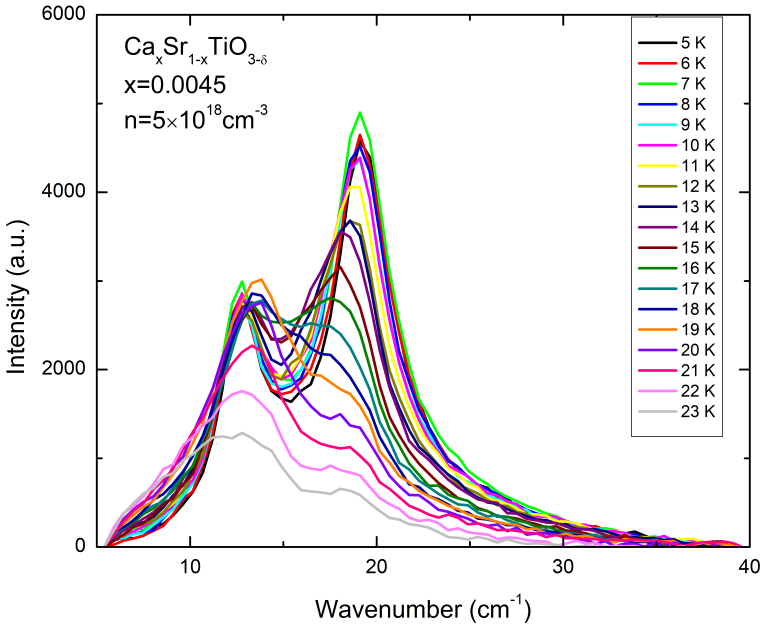

Figure 5.7: Raman spectra (after a linear background subtraction) of $Ca_xSr_{1-x}TiO_{3-\delta}$, for $x = 0.0045$ and $n = 5 \times 10^{18}\text{cm}^{-3}$.

and $n = 5 \times 10^{18}\text{cm}^{-3}$) are reported, with a background linear subtraction. Instead of only one, two peaks arise; this fact can be explained considering that there can be multiple domains in the ferroelectric state, each giving a different frequency. From the literature [42] [24], it is known that samples can be cut in a particular direction in order to favour a single orientation, so that the physical interpretation can be more clear.

In figure 5.8, it is possible to observe that the mode hardens when the temperature is below the Curie temperature. For the electron-doped sam-

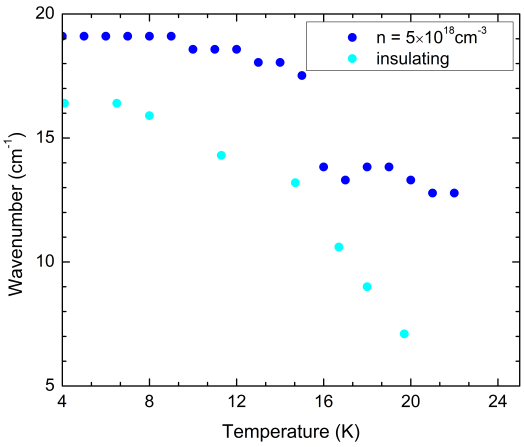

Figure 5.8: TO1 mode frequency as a function of temperature of $Ca_xSr_{1-x}TiO_{3-\delta}$, for $x = 0.0045$.

ples, only the case with $n = 5 \times 10^{18}\text{cm}^{-3}$ has been reported. In fact, as shown in figure 5.1, it is possible to see that for the most doped sample ($n = 1 \times 10^{19}\text{cm}^{-3}$) the anomaly temperature is at zero K, thus it is not in its ferroelectric-like phase and the soft phonon remains Raman inactive. On the other hand, for the least doped sample, a behaviour similar to the insulating sample is expected.
Moreover, due to the double peaks discussed above, the soft phonon frequency cannot be exactly determined.

CHAPTER 6

Discussion of results

In this chapter, the analysis of the measurements is discussed. In the first section, the phonon analysis is out, comparing the Reffit model to experimental data. In the second part, starting from optical conductivity, spectral weights are analysed and the effective mass for the metallic samples is computed.

6.1 Phonon analysis: temperature scan

In the following, Reffit models with lorentzian or Fano-shape[1] oscillators are used.
In this section, Reffit fits with reflectivity raw data are shown and it is explained how the optical conductivity from Reffit model can be compared to the optical conductivity computed via Kramers-Kronig relations.
In order to apply Kramers-Kronig relations, it is necessary to know reflectivity in the whole spectral range $(0, +\infty)$. But it is possible to make some approximations since the data are only available from $20 \sim 30\text{cm}^{-1}$ to 8000cm^{-1}: for higher wavenumbers the reflectivity can be considered

[1] A lorentzian oscillator gives a contribution to the dielectric function in the form

$$\epsilon(\omega) = [1+]\frac{\omega_p^2}{\omega_0^2 - \omega^2 - i\gamma\omega} \tag{6.1}$$

while for a Fano-shape oscillator, the function $\epsilon(\omega)$ is given by

$$\epsilon(\omega) = \frac{\omega_p^2}{\omega_0^2 - \omega^2 - i\gamma\omega}\left(q + i\frac{\omega_q}{\omega}\right)^2 + \left(\frac{\omega_p\omega_q}{\omega_0\omega}\right)^2 \tag{6.2}$$

where ω_p is the plasma frequency, ω_0 the frequency of the excitation, γ the scattering rate and ω_q represents the asymmetry of the oscillator (the asymmetry parameter is $q = \frac{\omega_q}{\omega_0}$).

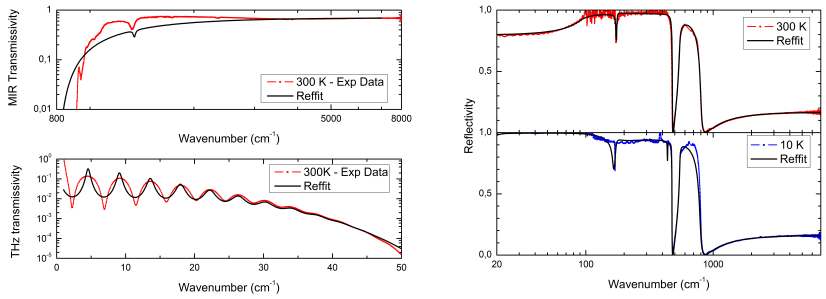

(a) Transmissivity *(b) Reflectivity*

Figure 6.1: Reffit model (black line) of $SrTiO_3$ compared to experimental spectra: 300 K in red and 10 K in blue.

constant, putting an oscillator at infinite frequency to make the optical conductivity an integrable quantity, while for lower wavenumbers the reflectivity can be taken from Reffit model and attached to the experimental spectrum.

6.1.1 $SrTiO_3$

As seen in the previous chapter, for $SrTiO_3$ also THz transmissivity and MIR transmissivity at room temperature are available, not only reflectivity spectra.
So, it is possible to exploit these three quantities at the same time to find the best fit at room temperature. Figure 6.1 presents the Reffit model, whose parameters are reported in table 6.1, and the measured experimental points. At first glance, we see that the worst fit is obtained for MIR transmissivity: indeed transmissivity is much more affected by defects than reflectivity, since the light has to pass through the whole sample. In agreement with the Lambert-Beer law, it is better to represent MIR transmissivity in a logarithmic scale, since the characteristic phenomena follow exponential behaviours. The aim of the fit is not only to reproduce the experimental data, but also to have a physical meaning. A perfect fit of the data could be obtained by increasing the number of oscillators in the model, however, without any physical meaning.
As shown in chapter 3, in the case of a perfect crystal, a model with Drude-Lorentz oscillators can be used to write the dielectric function where the oscillators describe the excitations of the structure, i.e., phonons. In figure 6.3, it is possible to observe that the ferroelectric soft phonon plays a crucial role and it shifts from 94cm^{-1} to around 20cm^{-1} when the temperature is 10 K, while in figure 6.2 is possible to see the gradual shift in the reflectivity spectra. The phonons TO2 and TO4 do not move with decreasing temperature and they contribute less also to the optical conductivity. The AFD

$SrTiO_3$ - 300 K

ω_0 (cm^{-1})	ω_p (cm^{-1})	γ (cm^{-1})	ω_q(cm^{-1})
93.6	1623.8	21.653	0.25522
175.5	300	2.1969	2.7
545	680.45	13.896	-35
1314	15.3	11.324	0

$SrTiO_3$ - 10 K

ω_0 (cm^{-1})	ω_p (cm^{-1})	γ (cm^{-1})	ω_q(cm^{-1})
21	1406	2.4968	0
171	335.07	6.12	0
176.35	664.75	139.41	0
438	36.108	3.3799	0
547.16	673.1	8.2527	-38.451

Table 6.1: Reffit model parameters of $SrTiO_3$ used in figure 6.1.

peak observed in reflectivity spectrum is not visible due to its tiny strength.

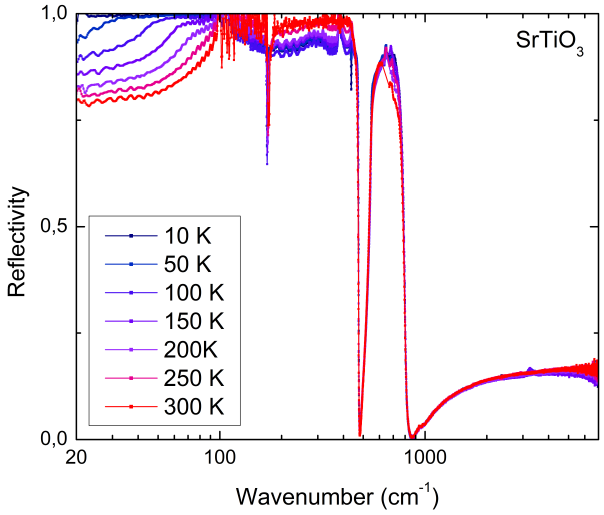

Figure 6.2: Reflectivity of $SrTiO_3$: spectra temperature dependence.

It is then possible to compare the real part of the optical conductivity computed via Kramers-Kronig relations and that one coming from the Reffit model. Figure 6.3b shows that the shape of the peaks is well described by lorentzian oscillators in the dielectric function, in particular at low temper-

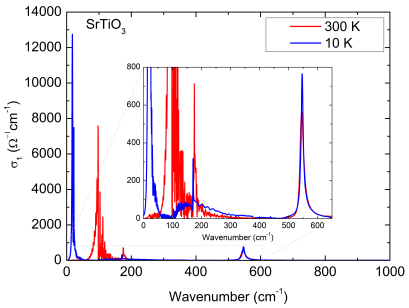

(a) σ_1 computed via Kramers-Kronig relations.

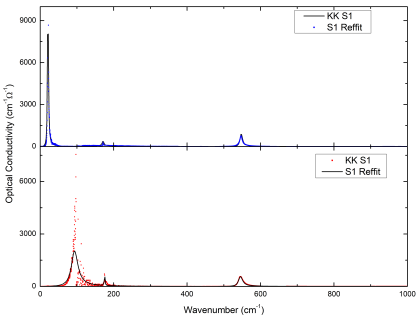

(b) σ_1 from Reffit model.

Figure 6.3: Real part of the optical conductivity σ_1 of $SrTiO_3$.

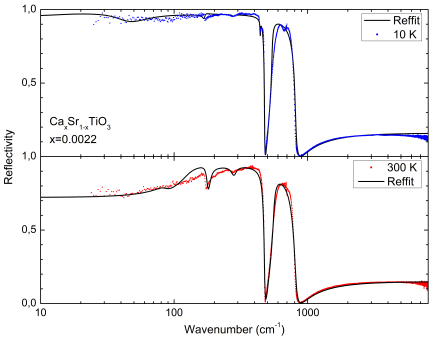

(a) $Ca_xSr_{1-x}TiO_3$ with $x = 0.0022$.

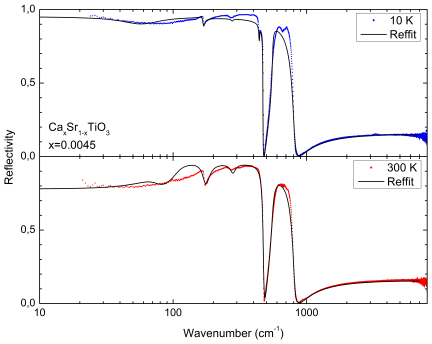

(b) $Ca_xSr_{1-x}TiO_3$ with $x = 0.0045$.

Figure 6.4: Reflectivity spectra at 10 K (blue) and 300 K (red) and respective Reffit models (black line) of $Ca_xSr_{1-x}TiO_3$.

ature.

Another feature of the Kramer-Kronig optical conductivity that is worth mentioning is the noise: in addition to experimental noise, as seen in equation 3.38, its amplification arises when reflectivity is close to one. Thus, with Kramers-Kronig relation is possible to keep track of the noise coming from the measurements.

6.1.2 $Ca_xSr_{1-x}TiO_3$: insulating samples

As illustrated in table 5.1, two insulating $Ca_xSr_{1-x}TiO_3$ samples with different Ca concentration x were measured: $x = 0.22\%$ and $x = 0.45\%$.

In both figures 6.4a and 6.4b, the reflectivity spectra and the Reffit curves are shown. It is possible to see that the fits, despite Fano-shape oscillators, cannot reproduce exactly the experimental points, in particular around TO2 phonon at 180cm^{-1}. From the reflectivity spectra it is more difficult to see

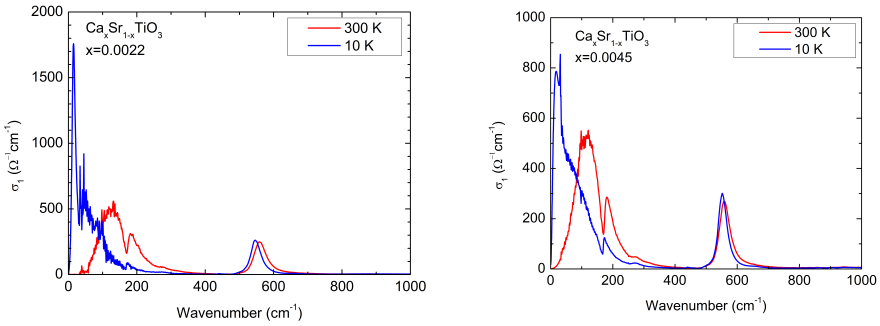

(a) $Ca_xSr_{1-x}TiO_3$ *with* $x = 0.0022$. *(b)* $Ca_xSr_{1-x}TiO_3$ *with* $x = 0.0045$.

Figure 6.5: Real part of the optical conductivity σ_1 computed via Kramers-Kronig relations (in blue 10 K and in red 300 K).

how the frequency of phonons changes with respect to $SrTiO_3$, while their behaviour is more evident looking at the real part of the optical conductivity (σ_1). In order to fit the experimental points, it was necessary to put a constraint on the zero-frequency conductivity (σ_{DC}), which is zero since these samples are insulating. In figures 6.5a and 6.5b, it is possible to see the broadening of the peaks with respect to lorentzian peaks in $SrTiO_3$ (in figure 6.3b). The broadening is due to Ca substitution: Sr atoms are randomly replaced by Ca atoms and this leads to defects in the crystal structure, due to inhomogeneities in the periodic structure; thus it is possible to speak of inhomogeneous broadening [43].
Considering the low temperature optical conductivity in figure 6.5, it is possible to see that the lorentzian oscillator (or Fano-shaped oscillator) cannot model the excitation due to its irregular shape. So, in the following part only the optical conductivity computed via Kramers-Kronig relations is considered.

Comparing the real part of the optical conductivity between $SrTiO_3$ and $Ca_xSr_{1-x}TiO_3$ samples, it is possible to spot some analogies and some other differences. Firstly the softening of the TO1 broad mode is clearly visible also in the Ca substituted sample, where the presence of the strong peak is due to Reffit model which extends the experimental spectrum below the measurement limit[2].

6.1.3 $Ca_xSr_{1-x}TiO_{3-\delta}$: electron-doped samples

Once understood how the optical conductivity changes as a function of the Ca concentration x, it is possible to fix $x = 0.45\%$ and consider different

[2]In the case of $Ca_xSr_{1-x}TiO_{3-\delta}$ samples, the measurement limit is around 25cm^{-1}, due to the smaller size of the samples, i.e. to larger noise.

samples with different carrier concentrations n. As explained in the first chapter, the electron doping of these samples is based upon oxygen removal in an annealing oven. As reported in table 5.1, three samples with the following electron density were measured: 9.2×10^{17}, 5×10^{18}, 10^{19} cm^{-3}.

For these samples, DC conductivity as function of temperature was known from previous work [25] and these values were used as a constraint to fit with the Reffit models the experimental points.
The reflectivity fits in figures 6.6a, 6.7a, 6.8a present the same problem of inhomogeneous broadening as in the previous case of the insulating samples, i.e. to improve the fits is necessary to add oscillators at low wavenumbers. All the fits were done up to the same level of discrepancy with experimental data. But to better understand the different behaviour it is easier to analyse and compare the optical conductivity. In figures 6.6b, 6.7b, 6.8b, it is possible to observe how the Drude peak increases with increasing the electron-doping, despite its small width. On the other hand, for the soft phonon a broadening occurs as in the case of insulating samples.

6.2 Spectral Weight and effective charge

As explained in chapter 3, it is possible to define the spectral weight, computed as follows:

$$W = \int_0^\infty \sigma_1(\omega) d\omega \tag{6.3}$$

where $\sigma_1(\omega)$ is the real part of the optical conductivity.
From experimental measurements, it is possible to cover just a finite energy range, up to a given energy cutoff (ω_c), so it is more appropriate to define the previous quantity as

$$W(\omega_c) = \int_0^{\omega_c} \sigma_1(\omega) d\omega \tag{6.4}$$

where the total spectral weight can be written as $W(\infty)$.
As described in chapter 3, it is possible to link the spectral weight to the material properties through the *f-sum rule*, which reads in CGS units:

$$W = \frac{\omega_p^2}{8} \tag{6.5}$$

where ω_p is the plasma frequency in CGS units, usually defined as $\omega_p^2 = \frac{4\pi N e^2}{m}$, with N density of electrons, e the elementary charge and m the mass of electrons.
When a complex structure as $Ca_xSr_{1-x}TiO_3$ is considered and if the cutoff

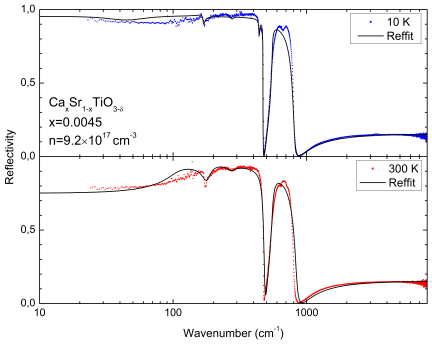

(a) Reflectivity spectra and Reffit models (black line).

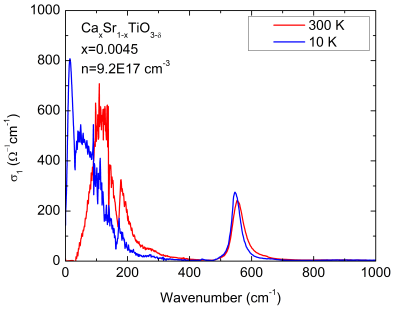

(b) Real part of the optical conductivity σ_1 at 300K (red) and 10 K (blue) from Kramers-Kronig relations.

Figure 6.6: $Ca_xSr_{1-x}TiO_{3-\delta}$ with $x = 0.0045$ and $n = 9.2 \times 10^{17}\mathrm{cm}^{-3}$.

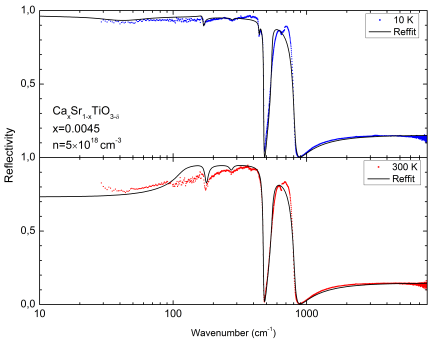

(a) Reflectivity spectra and Reffit models (black line).

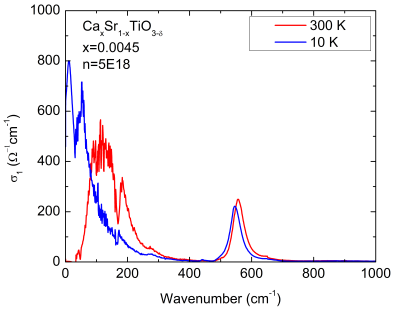

(b) Real part of the optical conductivity σ_1 at 300K (red) and 10 K (blue) from Kramers-Kronig relations.

Figure 6.7: $Ca_xSr_{1-x}TiO_{3-\delta}$ with $x = 0.0045$ and $n = 5 \times 10^{18}\mathrm{cm}^{-3}$.

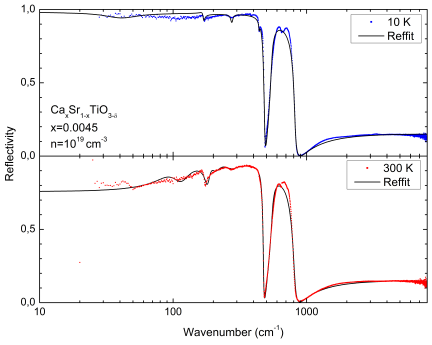

(a) Reflectivity spectra and Reffit models (black line).

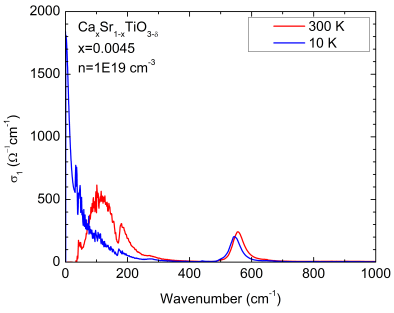

(b) Real part of the optical conductivity σ_1 at 300K (red) and 10 K (blue) from Kramers-Kronig relations.

Figure 6.8: $Ca_xSr_{1-x}TiO_{3-\delta}$ with $x = 0.0045$ and $n = 10^{19}\mathrm{cm}^{-3}$.

frequency is below the energy gap (which is $E_{gap} = 3.2\text{eV}$), it is possible to generalize the previous f-sum rule:

$$W = \frac{\omega_p^2}{8} = \sum_i \frac{\pi n_i Z_i^2 e^2}{2m_i} \tag{6.6}$$

where the sum is over all the atoms, n_i is their density, Z_i the effective charge and m_i their mass. Working again on this expression, it is possible to reshape it as

$$W = \frac{\pi e^2}{2\Omega} \sum_i \frac{Z_i^2 N_i}{m_i} \tag{6.7}$$

where Z_i is the oxidation number of each element, Ω the volume of the unit cell and N_i the number of atoms inside the unit cell.
In the case of $Ca_xSr_{1-x}TiO_3$, it is possible to write the sum in eq. 6.7 as follows

$$\sum_i \frac{Z_i^2 N_i}{m_i} = \frac{x Z_{\text{Ca}}^2}{m_{\text{Ca}}} + \frac{(1-x) Z_{\text{Sr}}^2}{m_{\text{Sr}}} + \frac{Z_{\text{Ti}}^2}{m_{\text{Ti}}} + \frac{3 Z_{\text{O}}^2}{m_{\text{O}}} \tag{6.8}$$

while the volume of the unit cell (cubic) can be computed as $\Omega = a^3$ where $a = 3.905\text{Å}$ is the lattice parameter.

Using eqs. 6.5 and 6.7, the theoretical spectral weight for the samples can be computed and thus the plasma frequency:

$$\omega_p^2(\omega_c) = 8W(\omega_c) = 4\pi \frac{e^2}{\Omega} \sum_i \frac{Z_i^2 N_i}{m_i} \tag{6.9}$$

In order to compute the spectral weight from the optical conductivity calculated via Kramers-Kronig relations, we need to recast the quantity in CGS units. In fact, the computed optical conductivity is in the units $\Omega^{-1}\text{cm}^{-1}$. We can write that the plasma frequency is

$$\omega_p^2 = 8 \int \sigma_1[CGS] d\omega = 8 \frac{2\pi c}{4\pi\epsilon_0} \int \sigma_1[\Omega^{-1}\text{cm}^{-1}] d\tilde{\nu} = \frac{4c}{\epsilon_0} \int \sigma_1^{\text{exp}} d\tilde{\nu} \tag{6.10}$$

where ν represents wavenumber in cm^{-1} and σ_1^{exp} is the real part of the optical conductivity found with Kramers-Kronig relations, expressed in $\Omega^{-1}\text{cm}^{-1}$. Instead of representing the spectral weight, it is possible to plot the square of plasma frequency as a function of energy.

6.2.1 $SrTiO_3$

Let us start the analysis of the spectral weight from $SrTiO_3$.

In figure 6.9a, it is clearly visible the transfer of spectral weight to lower wavenumbers with decreasing temperature, representing the softening of the

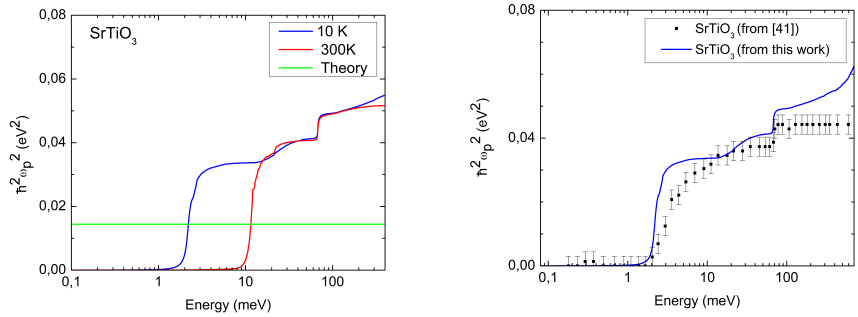

(a) In blue 10 K and in red 300 K.

(b) Comparison with previous results [41] at low temperature (10 K).

Figure 6.9: The square of the plasma frequency $\hbar^2\omega_p^2$ as function of energy of $SrTiO_3$.

ferroelectric TO1 phonon. This phonon is mostly responsible for the spectral weight, suggesting an important electron-phonon coupling.
Comparing to the results from previous work [41], it is possible to find an agreement on the order of magnitude of the plasma frequency, which gives consistency to the analysis.

In figure 6.9a, the green line represents the theoretical value ($\hbar^2\omega_p^2 = 0.0144\text{eV}^2$) computed from the f-sum rule, which is more or less three time smaller than the experimental value. This means that the material is not well-described by the ionic model, in fact in this case it is possible to speak of a charged phonon, i.e. in $SrTiO_3$ a strong electron-phonon coupling shows. The mentioned charged phonon is a complex excitation which includes the TO1 mode (i.e. the vibration of Ti against the oxygen octahedra) and electronic excitations from the lower band related to the oxygen orbitals 2p to the empty band associated to Ti 3d orbitals. It means that the vibration of the Ti atoms is linked to a change of the electron cloud, thus leading to a possible electric dipole.

6.2.2 $Ca_xSr_{1-x}TiO_3$: insulating samples

In figure 6.10, the spectral weights of the insulting Ca-substituted samples are represented. It is interesting to understand how the spectral weight changes from the $SrTiO_3$ sample to the Ca-substituted ones. As already seen, due to inhomogeneous broadening of the phonons, in particular the soft mode, a smoother step of the plasma frequency is expected.
In figure 6.11, it is possible to see that as the Ca concentration increases, the spectral weight increases more slowly than in the stoichiometric material, which is equivalent to say that the peak related to that phonon broadens.
What is worth underlining is that the total spectral weight remains the same

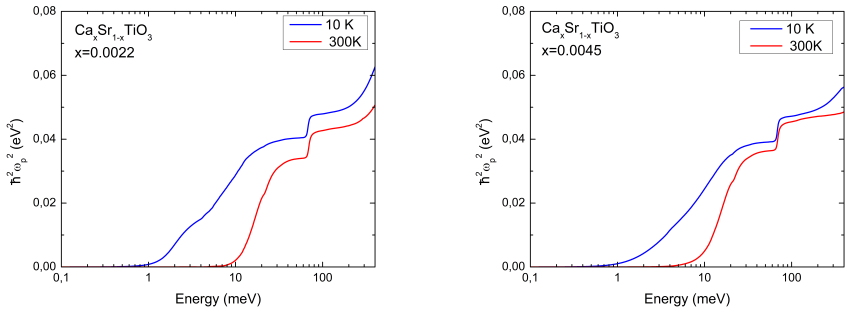

(a) $Ca_xSr_{1-x}TiO_3$, x=0.0022 *(b) $Ca_xSr_{1-x}TiO_3$, x=0.0045*

Figure 6.10: The square of the plasma frequency $\hbar^2\omega_p^2$ as function of energy at 10 (blue) and 300 K (red).

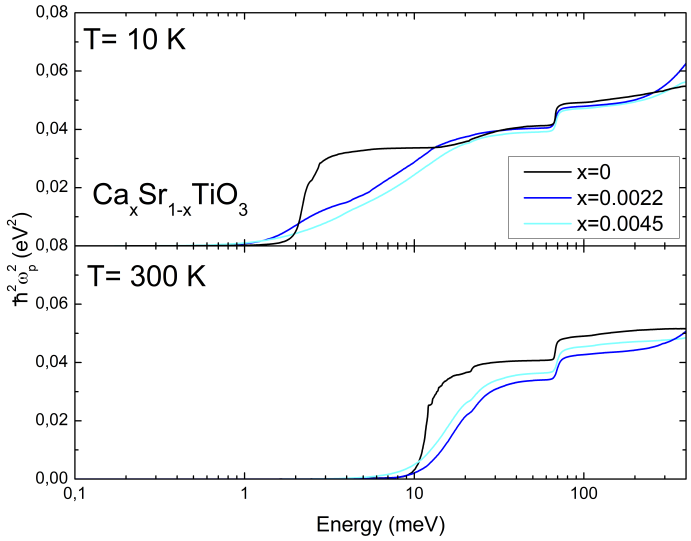

Figure 6.11: The square of the plasma frequency computed from the spectral weight of $Ca_xSr_{1-x}TiO_3$ for all the insulating samples: $x = 0$, $x = 0.0022$, and $x = 0.0045$.

in stoichiometric $SrTiO_3$ and in $Ca_xSr_{1-x}TiO_3$, which means that the spectral weight of the narrow TO1 phonon of $SrTiO_3$ transfers exactly to the spectral weight of the broader excitation of $Ca_xSr_{1-x}TiO_3$.

6.2.3 $Ca_xSr_{1-x}TiO_{3-\delta}$: electron-doped samples

In the following section, the spectral weight of $Ca_xSr_{1-x}TiO_{3-\delta}$ are presented, for a fixed Ca concentration x=0.0045.

In figure 6.12, it is possible to observe that at low temperature the spectral weight coming from the Drude peak increases as the carrier concentration increases. On the other hand, the same broad peak is found in all the metallic samples.

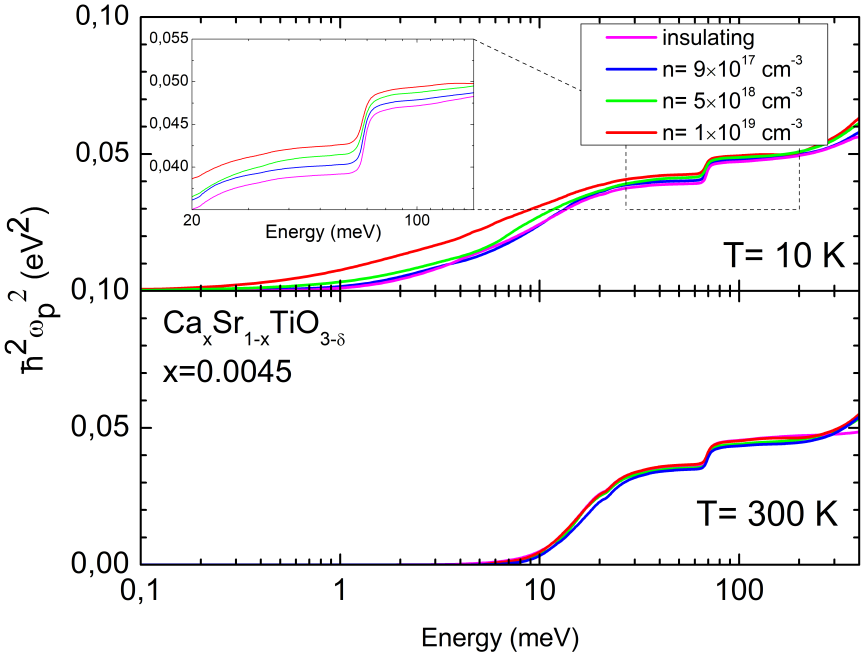

Figure 6.12: The square of the plasma frequency $\hbar^2\omega_p^2$ of $Ca_xSr_{1-x}TiO_{3-\delta}$, with x=0.0045 at 10 and 300 K.

It is possible to link this broad excitation to the ferroelectric-like order discussed in chapter one. If the picture of local electric dipoles holds, it would lead to an anisotropic environment for the Ti atoms, thus consistent with the observed broadening.

6.3 Effective mass

In metallic samples, it is possible to apply the f-sum rule to compute the effective mass of the electrons. In fact, if there are free electrons, the eq. 6.9 can be written as

$$\omega_p^2 = 4\pi \frac{e^2}{\Omega} \sum_i \frac{Z_i^2 N_i}{m_i} + \frac{4\pi e^2 n_{\text{carriers}}}{m_{\text{eff}}} \tag{6.11}$$

where, in the last term, n_{carriers} is the free carrier concentration and m_{eff} the effective mass of the carriers. The theoretical spectral weight, as already seen, is smaller than the experimental one, so instead of considering the theoretical value, it makes sense to use the experimental value, leading to the expression:

$$\omega_p^2 = \omega_{p,\text{insulating}}^2 + \frac{4\pi e^2 n_{\text{carriers}}}{m_{\text{eff}}} \tag{6.12}$$

Thus, it is possible to subtract the contribution of the phonons for the spectral weight to compute the Drude spectral weight and thus the effective mass of the carriers. In order to find the effective mass, it is necessary to fix a cutoff energy: it is possible to choose this point looking to where the spectral weight presents a plateau. From the inset in figure 6.12, two possible frequencies can be 60 and 100meV. The difference between this two values is mostly influenced by the TO4 mode around 550cm^{-1},i.e., 70meV.

Table 6.2 reports the computed effective mass for these two energy.
For both the cutoff energies, the effective mass increases with increasing

E_{cutoff} (meV)	n_{carriers} (cm^{-3})	m_{eff} (m_e)	Δm_{eff} (m_e)
60	9.2×10^{17}	1.14	1.00
60	5×10^{18}	3.00	1.29
60	10^{19}	3.97	1.14
100	9.2×10^{17}	1.83	1.25
100	5×10^{18}	4.44	1.36
100	10^{19}	6.25	1.35

Table 6.2: Effective mass of the free carriers computed from the spectral weight, for $Ca_xSr_{1-x}TiO_{3-\delta}$ with $x = 0.0045$.

the electron densities. It is interesting to compare the computed values to the effective mass values found in the case of metallic $SrTiO_{3-\delta}$ [14].

Figure 6.13 shows the values of the effective mass as a function of the carrier concentration. It is possible to observe that the same behaviour was found in the case of $SrTiO_{3-\delta}$ [14], with similar magnitude. The errorbars have been estimated considering a relative error of reflectivity of 1%, then the propagation of the errors was carried out applying Kramers-Kronig relations.

Let us discuss what figure 6.13 shows. First, the points from this work confirm the presence of a maximum of the effective mass. This might be explained thinking that the system is in proximity of the Lifshitz transition[3], in fact the carriers density is near the critical level $n_{c,2}$, i.e., when the third

[3]A Lifshitz transition occurs when the topology of the Fermi surface changes e.g. a new band is filled.

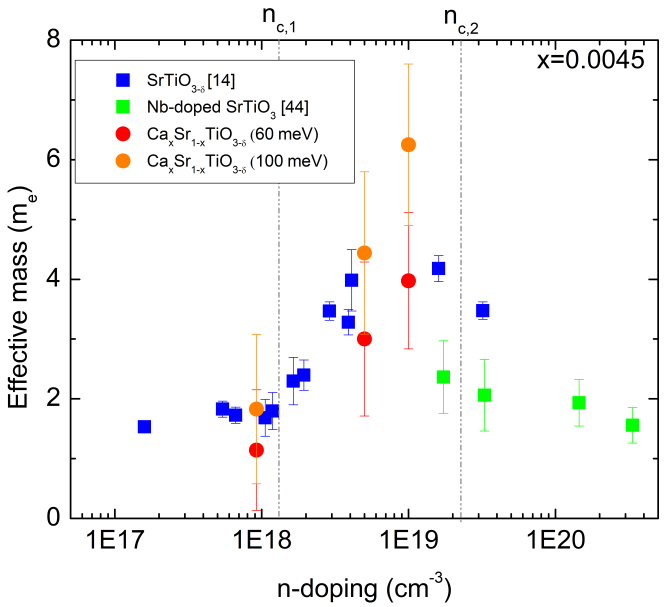

Figure 6.13: The computed effective mass m_{eff} of $Ca_xSr_{1-x}TiO_{3-\delta}$ with $x = 0.0045$ as a function of the carriers density n for two different cutoff energies (60 and 100 meV), compared to the effective mass of n-doped $SrTiO_3$, adapted from [14][44].

band starts to be filled.
It is possible to find an expected behaviour for the effective mass as a function of the carrier concentration in the context of a Fermi electron gas, which can be considered realistic when a band is almost empty.
Thus, it is possible to compute the ratio between the kinetic term:

$$< K > \sim \frac{\hbar^2 n^{2/3}}{2m_e} \tag{6.13}$$

and the potential term, assuming Coulomb interaction:

$$< V_c > \sim \frac{e^2}{n^{1/3}} \tag{6.14}$$

leading to the expression

$$\frac{< V_c >}{< K >} \sim \frac{2m_e e^2}{\hbar^2} n^{-1/3} \tag{6.15}$$

which means that already in this simple model a divergence is observed when the electron density (of the third band) becomes small enough.
Secondly, it is possible to say that the ferroelectric-like order does not affect too much the free electrons, since the mass enhancement is similar to the case of $SrTiO_{3-\delta}$ samples.

Conclusions and future outlook

In this work, the phonon properties of $SrTiO_3$ and $Ca_xSr_{1-x}TiO_{3-\delta}$ samples were studied by means of FTIR spectroscopy, in an energy range between 20 and 8000cm^{-1} between 10 and 300 K. The Ca-substituted samples were characterised by two different Ca concentrations x ($x = 0.0022$ and $x = 0.0045$) and three different carrier densities n for $x = 0.0045$ ($n = 9.2 \times 10^{17}, 5 \times 10^{18}, 1 \times 10^{19}$cm^{-3}).

Firstly, measurements on $SrTiO_3$ were taken and were compared to results from previous studies. A measurement procedure was established, in order to fix the experimental parameters and obtain comparable data.
By looking at the spectral weight W it is possible to confirm that $SrTiO_3$ shows a strong electron-phonon coupling: the experimental value of W is more or less 3 times bigger than the theoretical one, suggesting that the pure ionic picture is not appropriate. In agreement with previous data, most of the spectral weight is related to the ferroelectric soft mode, associated to the the vibration of Ti atoms against oxygens octahedra.

Secondly, the analysis of $Ca_xSr_{1-x}TiO_{3-\delta}$ was carried out.
A broadening of the peak associated to the soft phonon is observed, with the exact transfer of spectral weight in the case of the insulating samples with respect to the stoichiometric $SrTiO_3$.
This phenomenon can be related to the loss of translational symmetry due to the random substitution of Sr atoms with Ca atoms: Ti atoms find different environments. This leads to the so-called inhomogeneous broadening.

Qualitatively, to explain the increase of the peak width, it is also possible to think of the double-well potential of the Ti atom with discrete energy levels. The state is not excited in a single process, but it can undergo different jumps in energy. From the peak width, it can be possible to model the energy

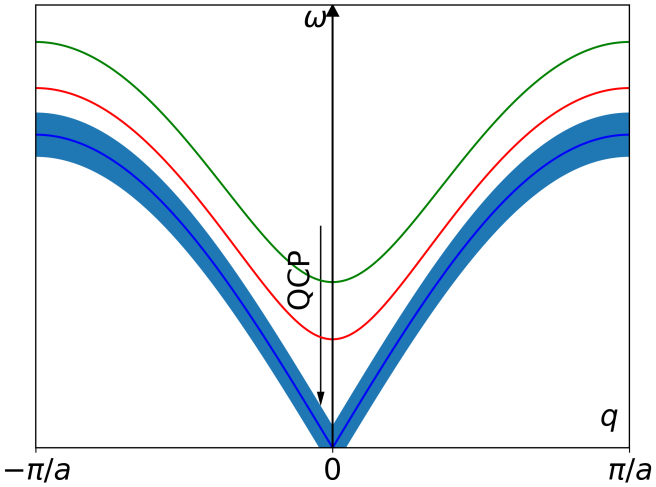

Figure 6.14: Dispersion relations of a possible ferroelectric soft mode in a quantum critical scenario, as a function of the tuning parameter. The blue area represents the uncertainty of the wavevector q.

differences between the levels, considering a Gibbs ensemble with its associate probability of finding a populated level. Once that the energy levels are computed, a double well potential characterised by those levels can be found.

Moreover, in the case of $Ca_xSr_{1-x}TiO_3$ samples, at low temperature the material exhibits a percolating ferroelectricity, although the softening of the phonon remains incomplete, as shown in Raman measurements. This might be another cause for the broadening.

Due to the broadening of the soft phonon, it is not possible to define the peak in the optical conductivity as a precise mode in Ca-substituted samples, thus $\boldsymbol{q}$ is not a good quantum number. Qualitatively, it is possible to visualise the uncertainty of $\boldsymbol{q}$ as the blue area in figure 6.14, where the blue line represents the dispersion relation. In order to apply the quantum critical scenario presented in [29] to Ca-substituted samples, the role of this uncertainty has to be discussed and further investigations are needed.

In metallic $Ca_xSr_{1-x}TiO_{3-\delta}$, the same broadening of the soft phonon was observed. The Drude peak was fitted using the constraint of DC conductivity. For these samples, the effective mass of the free carriers was computed, showing an agreement with the effective mass of $SrTiO_{3-\delta}$ found in previous works. It turns out the Ca-substitution does not affect the free carrier mass.

The effective mass as function of carrier concentration attains its maximum around $n \simeq 10^{19}\text{cm}^{-3}$. Since it is known that in n-doped $SrTiO_3$ the effective mass decreases for higher carrier concentrations, it can be interesting to measure $Ca_xSr_{1-x}TiO_{3-\delta}$ samples with higher electron doping to see if the same dome as a function of electron density occurs.

In summary, a broadening of the ferroelectric soft phonon associated to the Ca-substitution was measured and an increase of the effective mass as a function of carrier concentration was found in the metallic samples.

Bibliography

[1] E. K. H. Salje et al. "The cubic-tetragonal phase transition in strontium titanate: excess specific heat measurements and evidence for a near-tricritical, mean field type transition mechanism". In: *Journal of Physics: Condensed Matter* 10.25 (1998), p. 5535.

[2] D. van der Marel, J. L. M. van Mechelen, and I. I. Mazin. "Common Fermi-liquid origin of T^2 resistivity and superconductivity in n-type $SrTiO_3$". In: *Phys. Rev. B* 84 (20 2011), p. 205111.

[3] K. A. Müller and H. Burkard. "$SrTiO_3$: An intrinsic quantum paraelectric below 4 K". In: *Phys. Rev. B* 19 (7 1979), pp. 3593–3602.

[4] P. A. Fleury, J. F. Scott, and J. M. Worlock. "Soft Phonon Modes and the 110 K Phase Transition in $SrTiO_3$". In: *Phys. Rev. Lett.* 21 (1 1968), pp. 16–19.

[5] Y. Yamada and G. Shirane. "Neutron Scattering and Nature of the Soft Optical Phonon in $SrTiO_3$". In: *Journal of the Physical Society of Japan* 26.2 (1969), pp. 396–403.

[6] J. F. Schooley, W. R. Hosler, and Marvin L. Cohen. "Superconductivity in Semiconducting $SrTiO_3$". In: *Phys. Rev. Lett.* 12 (17 1964), pp. 474–475.

[7] J. F. Schooley et al. "Dependence of the Superconducting Transition Temperature on Carrier Concentration in Semiconducting $SrTiO_3$". In: *Phys. Rev. Lett.* 14 (9 1965), pp. 305–307.

[8] C. S. Koonce et al. "Superconducting Transition Temperatures of Semiconducting $SrTiO_3$". In: *Phys. Rev.* 163 (2 1967), pp. 380–390.

[9] X. Lin et al. "Fermi Surface of the Most Dilute Superconductor". In: *Phys. Rev. X* 3 (2 2013), p. 021002.

[10] A. Ohtomo and H. Y. Hwang. "A high-mobility electron gas at the $LaAlO_3/SrTiO_3$ heterointerface". In: *Nature* 427 (Jan. 2004), p. 423.

[11] N. Reyren et al. "Superconducting Interfaces Between Insulating Oxides". In: *Science* 317.5842 (2007), pp. 1196–1199. ISSN: 0036-8075.

[12] K. Behnia. "On mobility of electrons in a shallow Fermi sea over a rough seafloor". In: *Journal of Physics: Condensed Matter* 27.37 (2015), p. 375501.

[13] P. P. Edwards and M. J. Sienko. "Universality aspects of the metal-nonmetal transition in condensed media". In: *Phys. Rev. B* 17 (6 1978), pp. 2575–2581.

[14] X. Lin et al. "Critical Doping for the Onset of a Two-Band Superconducting Ground State in $SrTiO_{3-\delta}$". In: *Phys. Rev. Lett.* 112 (20 2014), p. 207002.

[15] C. Collignon et al. "Metallicity and superconductivity in doped strontium titanate". In: *ArXiv e-prints* (Apr. 2018). arXiv: `1804.07067 [cond-mat.supr-con]`.

[16] G. Geneste and J. Kiat. "Ground state of Ca-doped strontium titanate: Ferroelectricity versus polar nanoregions". In: *Phys. Rev. B* 77 (17 2008), p. 174101.

[17] J. G. Bednorz and K. A. Müller. "$Sr_{1-x}Ca_xTiO_3$: An XY Quantum Ferroelectric with Transition to Randomness". In: *Phys. Rev. Lett.* 52 (25 1984), pp. 2289–2292.

[18] Y. G. Wang et al. "Impurity-induced phase transition in quantum paraelectrics". In: *Phys. Rev. B* 57 (21 1998), pp. 13343–13346.

[19] V. V. Lemanov et al. "Phase transitions and glasslike behavior in $Sr_{1-x}Ba_xTiO_3$". In: *Phys. Rev. B* 54 (5 1996), pp. 3151–3157.

[20] M. Itoh et al. "Ferroelectricity Induced by Oxygen Isotope Exchange in Strontium Titanate Perovskite". In: *Phys. Rev. Lett.* 82 (17 1999), pp. 3540–3543.

[21] H. Uwe and T. Sakudo. "Stress-induced ferroelectricity and soft phonon modes in $SrTiO_3$". In: *Phys. Rev. B* 13 (1 1976), pp. 271–286.

[22] J. Hemberger et al. "Electric-field-dependent dielectric constant and nonlinear susceptibility in $SrTiO_3$". In: *Phys. Rev. B* 52 (18 1995), pp. 13159–13162.

[23] M. A. Carpenter et al. "Structural relationships and a phase diagram for $(Ca, Sr)TiO_3$ perovskites". In: *Journal of Physics: Condensed Matter* 18.48 (2006), p. 10725.

[24] W. Kleemann et al. "Optical detection of symmetry breaking on a nanoscale in SrTiO3:Ca". In: *Ferroelectrics* 203.1 (1997), pp. 57–74.

[25] C. W. Rischau et al. "A ferroelectric quantum phase transition inside the superconducting dome of $Sr_{1-x}Ca_xTiO_{3-\delta}$". In: *Nature Physics* 13 (Apr. 2017), p. 643.

[26] S. S. Saxena et al. "Superconductivity on the border of itinerant-electron ferromagnetism in UGe2". In: *Nature* 406 (Aug. 2000), p. 587.

[27] J. H. Lee et al. "A strong ferroelectric ferromagnet created by means of spin–lattice coupling". In: *Nature* 466 (Aug. 2010), p. 954.

[28] S. E. Rowley et al. "Ferroelectric quantum criticality". In: *Nature Physics* 10 (Mar. 2014), p. 367.

[29] J. M. Edge et al. "Quantum Critical Origin of the Superconducting Dome in $SrTiO_3$". In: *Phys. Rev. Lett.* 115 (24 2015), p. 247002.

[30] A. Stucky et al. "Isotope effect in superconducting n-doped SrTiO3". In: *Scientific Reports* 6 (Nov. 2016), p. 37582.

[31] J. Valasek. "Piezo-Electric and Allied Phenomena in Rochelle Salt". In: *Phys. Rev.* 17 (4 1921), pp. 475–481.

[32] V. Fridkin and S. Ducharme. "Ferroelectricity and Ferroelectric Phase Transition". In: *Ferroelectricity at the Nanoscale*. NanoScience and Technology. Springer, Berlin, Heidelberg, 2014, pp. 1–9. ISBN: 978-3-642-41006-2 978-3-642-41007-9.

[33] R. E. Cohen. "Origin of ferroelectricity in perovskite oxides". In: *Nature* 358 (July 1992), 136 EP –.

[34] N.W. Ashcroft and N.D. Mermin. *Solid State Physics*. HRW international editions. Holt, Rinehart and Winston, 1976. Chap. 22,23,24. ISBN: 9780030839931.

[35] J. F. Scott. "Soft-mode spectroscopy: Experimental studies of structural phase transitions". In: *Rev. Mod. Phys.* 46 (1 1974), pp. 83–128.

[36] H. K. Onnes. "research notebooks 56, 57". In: *Kamerlingh Onnes Archive, Boerhaave Museum, Leiden, the Netherlands* (1911).

[37] V. L. Ginzburg and L. D. Landau. "On the Theory of superconductivity". In: *Zh. Eksp. Teor. Fiz.* 20 (1950), pp. 1064–1082.

[38] J. Bardeen, L. N. Cooper, and J. R. Schrieffer. "Theory of Superconductivity". In: *Phys. Rev.* 108 (5 1957), pp. 1175–1204.

[39] M. Dressel and G. Grüner. *Electrodynamics of Solids: Optical Properties of Electrons in Matter*. Cambridge University Press, 2002. DOI: 10.1017/CBO9780511606168.

[40] F. Gervais et al. "Temperature dependence of plasmons in Nb-doped $SrTiO_3$". In: *Phys. Rev. B* 47 (13 1993), pp. 8187–8194.

[41] J. L. M. van Mechelen. "Charge and Spin electrodynamics of SrTiO3 and EuTiO3 studied by optical spectroscopy". PhD thesis. 2010.

[42] U. Bianchi, W. Kleemann, and J. G. Bednorz. "Raman scattering of ferroelectric $Sr_{1-x}Ca_xTiO_3$, x=0.007". In: *Journal of Physics: Condensed Matter* 6.6 (1994), p. 1229.

[43] A. M. Stoneham. "Shapes of Inhomogeneously Broadened Resonance Lines in Solids". In: *Rev. Mod. Phys.* 41 (1 1969), pp. 82–108.

[44] J. L. M. van Mechelen et al. "Electron-Phonon Interaction and Charge Carrier Mass Enhancement in $SrTiO_3$". In: *Phys. Rev. Lett.* 100 (22 2008), p. 226403.

Acknowledgements

I would like to thank Prof. Ghiringhelli for his advice to contact Prof. van der Marel and for his suggestions regarding the future.
A special thank goes to Prof. van der Marel for accepting me as a master thesis student in his group in the DQMP at the University of Geneva, for his advice and the proposal for next years.
I want to express a sincere thank to my tutor Willem Rischau, not only for the approach to research he has taught me, but mostly for his patience, his passion and willingness to help me in my project. Furthermore, I would like to extend my thanks to all the group members for the inspiring and interesting discussions during lunch breaks as well as when I asked questions related to their research. I hope that in the following years I will have the opportunity to strengthen these relationships.

At the same time, I want to thank all my family, in particular my parents Maria Angela and Daniele, my brother Alessandro for their support and their trust, even if when it meant distance from home. Without them, I could not be here.
Thanks to all my friends from Milan: to Pietro and Pierdomenico, but also Raffaele, Marco, Federico, Giuseppe for their advice and strong friendship. To all my colleagues of Engineering Physics. To my friends from Lausanne. Along with them, I want to extend these thanks to all my friends from Parma, who are always available to get together for a dinner after few months, in particular to my friends from high school.

Eventually, I really want to thank Vittoria, because she has helped and encouraged me through these last two years, trusting me and accepting my trust. Thanks because she has given me the energy and the motivation to arrive here.

Thank you all, because I have become what I am just because I have met so many interesting and encouranging people.